Imperial College
London

Final Group Report for IBSc/MEng Group Project

Microfluidic Blood-Brain Barrier Chip for Glioblastoma Multiforme ImmunoPET Radiotracer Development

Author names:
Daniele Cotton, Callan Egan, Peter Guite, Hon Kwan Allan Lee, Jaynell Ng, Denis Sokolov

Supervisor: Dr Sam Au

Submitted in partial fulfilment of the requirements for the award of IBSc/MEng in Biomedical Engineering from Imperial College London

17th March 2021 Word count: 4941

Feedback box for project markers:

WHAT I liked about the report:
WHAT could/should be improved:

Covid Statement

For the benefit of the second marker, we have been asked to include a 300-word summary of the effect the Coronavirus pandemic has had on our group project progress up till this point.

I agree that that the below statement is truthful and accurate.
Dr Sam Au – Group Supervisor – 15.03.2021

The Coronavirus pandemic has negatively impacted the progress of this group project.

Though every effort has been made throughout the project research and design stages to work from home effectively and use computer software where applicable, our project is not a computational model and thus progress towards the fabrication, testing and integration of our physical device has been severely inhibited due to the pandemic. Our ambitious project draws on the work of three separate and heavily laboratory dependent activities, namely: microfabrication, cell culture and electrical sensing. The delay of the returns to labs has put an extraordinary squeeze on the time available to gather results relating to these three activities.

During a meeting on December 18th 2020 with Dr Sam Au, plans were put in place to continue with our group planning report - detailing the work we expected to do in university laboratories from mid to late January. Due to further restrictions implemented by the UK government and the necessity to complete safety inductions and training, which could have otherwise been completed much earlier in the project, we only gained full access to make progress on our project for the:

Imperial College Advanced Hackspace, White City campus, on February 17th
Tissue culture facility-(B114) on February 24th
Cardiovascular laboratory-(B106) on March 3rd
CRUK microfabrication facility-(B120) on March 12th

Despite high demand, the Advanced Hackspace is now also operating under reduced capacity, only available three days a week, which has further delayed 3D prints and use of a dark room needed by the electrical sensing team.

The group has worked incredibly hard to run experiments, fabricate parts and gather results, and special consideration should be given for the extremely short period in which all this was possible.

Abstract

Glioblastoma multiforme (GBM) is a common and aggressive brain cancer with a median survival rate of 15 months post-diagnosis. To improve clinical outcomes, immunoPET radiotracers can be used to inform personalised cancer treatment for each patient. This project aims to create an *in vitro* microfluidic device which replicates the selective permeability of the blood-brain-barrier (BBB). The device consists of an endothelial cell cultured microchannels, a collection reservoir and a photodiode sensing system. This integrated device is uniquely tailored to measuring the permeability of our *in vitro* barrier model to immunoPET radiotracers, with the goal of supporting further immunoPET radiotracer development for targeted GBM management.

The *in vitro* chip (barrier model and reservoir) layout has been designed and fabricated by moulding PDMS and will be seeded with endothelial cells. The photodiode used in the sensing system design has been tested with LEDs and will be implemented with the reservoir to measure the concentration of ImmunoPET which has passed through the model and thus assess the permeability of novel immunoPET radiotracers to the *in vitro* barrier model. The preferred cell line hCMEC/D3 became unavailable at short notice and HUVECs were selected as the best available alternative. Despite culturing the HUVECs from the moment the growth media arrived, they did not reach sufficient confluency by the time of this report. Substantial progress has been made in individual areas of the project suggesting that their integration will form a device that meets our success criteria.

Acknowledgements

Special thanks must go to all those who have helped in assisting our project.

Dr Sam Au, Group Supervisor, Department of Bioengineering at Imperial College London
Dr Phillip Miller, Senior Lecturer Department of Chemistry at Imperial College London
Dr Gabriela Kramer-Marek, Head of Preclinical Molecular Imaging at The Institute of Cancer Research
Harry Barnett, Hackspace Fellow at Imperial College London
Dr David Miller, Hackspace Fellow at Imperial College London
Dr David Labonte, Group Project Coordinator, Department of Bioengineering at Imperial College London

The authors also acknowledge Julian Ashby, Elizabeth Wheeler and Neelima KC, PhD students at Imperial College London, as well as Miguel Hermida for their advice and assistance with tissue culturing and microfabrication.

1. Introduction

1.1 Background

GBM

Glioblastoma multiforme (GBM) is a primary malignancy of the central nervous system that comprises 60% of all adult brain tumours[1][2]. GBM is lethal disease with an extremely poor prognosis; the median survival in GBM patients is 14-15 months from diagnosis[3]. GBM remains largely incurable and treatment failure often occurs due to the high molecular heterogeneity in GBM phenotype[2][4]. Personalised medicine is promising approach in improving outcomes for GBM patients[5]. Personalised medicine for cancer entails targeting therapies to each patient based on the unique genetic and molecular signatures of their tumour[5][6]. An imaging technique that enables clinicians to distinguish patient-specific molecular phenotypes *in vivo* may facilitate the development of novel targeted therapies for GBM[6][7].

ImmunoPET

Immuno-positron Emission Tomography (immunoPET) is the use of PET imaging with radioactively tagged antibodies acting as radiotracers. Uptake of this radiotracer will be increased in the antibodies' target area. Positrons emitted from these radiotracers decay into 511keV gamma photons and allow imaging of those target areas. For GBM, radiotracers must cross the blood-brain-barrier (BBB) in order to bind to tumour cells. Therefore, the highly restrictive barrier functionality of the BBB hinders the development of immunoPET agents[6][8].

BBB

The BBB is a neurovascular unit specialised to maintain brain homeostasis and prevent xenobiotics from entering the neuronal milieu[8]. The BBB is composed of brain capillary endothelial cells (BCECs), pericytes and astrocytic endfeet[8][9]. The BCECs of the BBB possess complex tight junctions (TJs), specific solute carriers, receptor-mediated transporters and ABC-type efflux transporters that facilitate the highly regulated transport of substances between the blood and central nervous system (CNS)[10]. The integrity of the BBB can be disrupted by tumours such as GBM, resulting in the formation of the blood-brain tumour barrier (BBTB). The BBTB is characterised by heterogenous permeability profile[8].

ImmunoPET Transport Across the BBB

Transport across endothelia may be either transcellular or paracellular[10]. There are two transcellular transport mechanisms by which immunoPET radiotracers may traverse the BCEC monolayer: adsorptive-mediated transcytosis (AMT) or receptor-mediated transcytosis (RMT). Paracellular transport of immunoPET agents across the BBB is inhibited by TJs between adjacent BCECs[11]. In addition, drugs that do traverse the BBB may be actively transported back into the capillary lumen by ABC-family efflux transports[12] . Hence, the presence of RMT and AMT transport systems, ABC-family efflux transporters and confluent monolayers with high junctional tightness are important properties for in vitro BBB models used for permeability screening studies[10][13].

In Vitro Microfluidic Models

To study the transport of molecules across the BBB, animal models are the most established *in vivo* methods since direct experimentation on the human brain is unethical. However, besides being costly and time-consuming[14], 50% of results obtained cannot be translated into correct human responses[4]. *In vitro* models overcome issues associated with animal experiments by (1) lowering costs and duration spent on experiments, (2) obtaining accurate results since human cells are used, and (3) being more ethical since no living organism is harmed. Referring to Figure 1, these models have 3 components – membrane, luminal compartment (hereinafter referred to as blood channel) and abluminal compartment[4][15] (hereinafter referred to as brain channel). There are 2 groups of *in vitro* models: static and dynamic, with dynamic models being able to introduce shear stress over cells using flow (Figure 3)[14]. Transwell systems are easily scalable but lack the three-dimensional structure and shear stress level experienced *in vivo*[15]. Being dynamic models, Dynamic *in vitro* (DIV) and microfluidic models can achieve physiological levels of barrier tightness[15]. DIV, however, prevents visual assessment of cell growth such as fluorescence and confocal microscopy due to the opaque polypropylene fibres[14][15]. Microfluidics have yet to have a standardised quantification of parameters but show promise since they are better able to mimic brain microenvironments compared to DIV models[15] and can be manufactured rapidly at low costs[15].

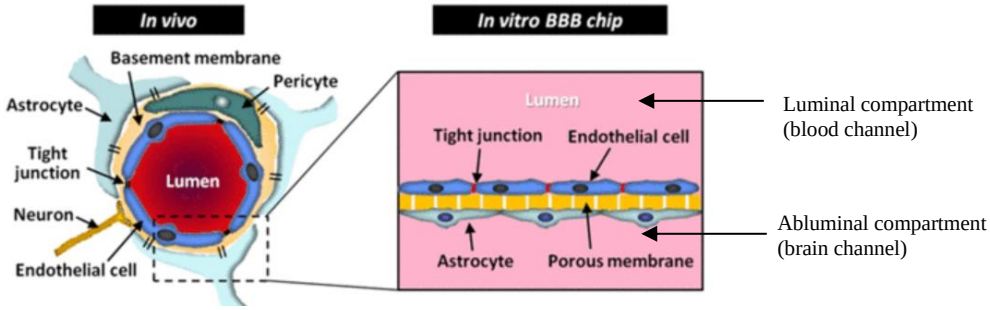

Figure 1: Comparison of physiological (*in vivo*) BBB with *in vitro* BBB models. The 3 main components are the luminal compartment (blood channel), abluminal compartment (brain channel) and the membrane. Figure adapted from Jeong[18].

Shear Stress

Shear stress (SS) promotes barrier tightness through increased TJ proteins expression of BMECs[16]. It also ensures a confluent monolayer of cells[17]. For brain capillaries of 10µm in diameter with blood viscosity being 4mPa·s and flow rate of 6-12nL/min, SS experienced by BCECs is 10-20dyn/cm^2[17] which *in vitro* models should aim to achieve. However, a study showed that SS of 1dyn/cm^2 can achieve 85% of highest barrier integrity measured when SS is 20dyn/cm^2 (Figure 2)[18]. Hence, it was hypothesised that *in vitro* models should minimally achieve a SS of 1dyn/cm^2 to provide conditions for a physiologically representative barrier. However, overly high SS (>30dyn/cm^2) reduces cell adhesion and hence barrier integrity[18].

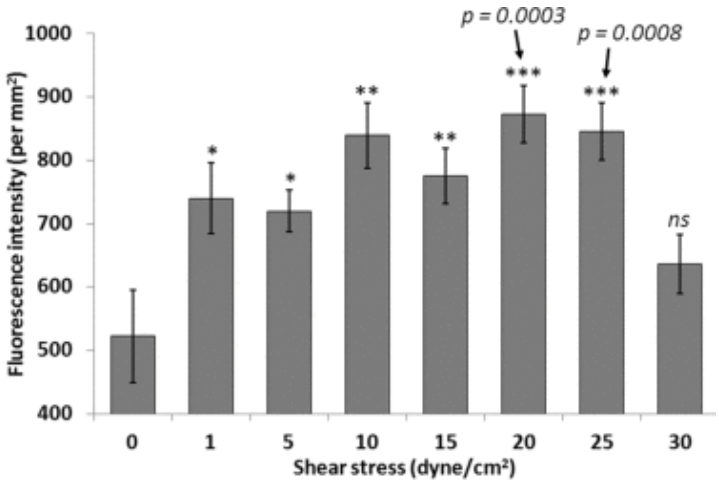

Figure 2: A graph showing the relationship between shear stress and barrier integrity, which is represented by fluorescence intensity. The higher the fluorescence intensity, the higher the degree of ZO-1 expression, which means higher degree of tight junction formation and hence a tighter barrier formed. Figure adapted from Jeong[18].

Validation Markers for *in vitro* BBB models

The presence of confluent monolayers with continuous TJs can be validated by immunocytochemistry to localise TJ proteins[10]. The integrity of the barrier can be validated by performing permeability assays with fluorescently labelled tracer molecules of different molecular sizes or by measuring Trans-endothelial electrical resistance (TEER)[10]. Both are needed to test permeability of large and small molecules to the BBB respectively. *In vivo* human TEER value is 1500-8000Ω·cm^2, with 150Ω·cm^2 being the lowest acceptable value for *in vitro* models[4]. As each method may be compromised by experimental design (such as the handling of cells during experiments), a robust evaluation of paracellular permeability involves assessment of both tracer molecule flux and TEER[10].

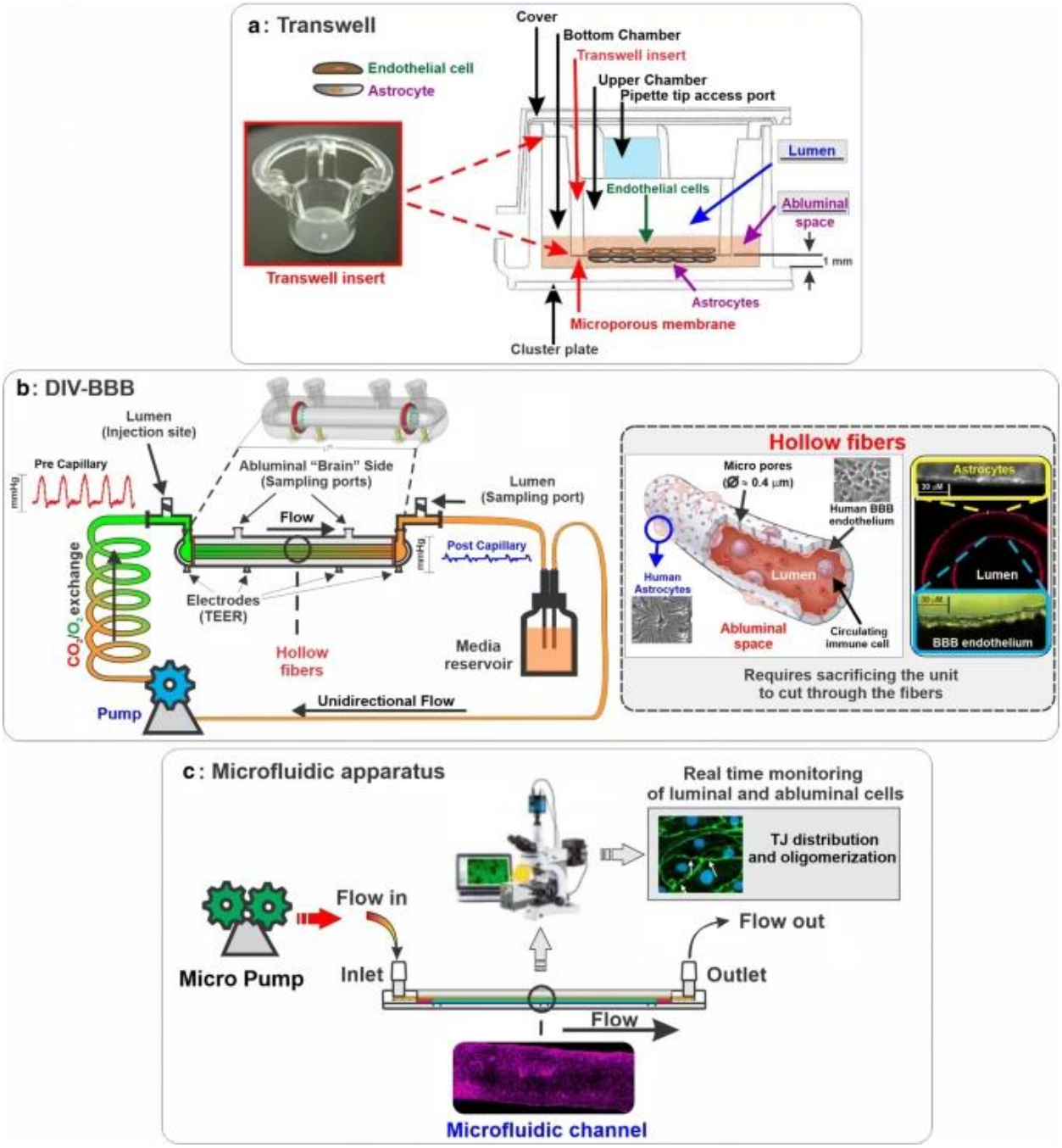

Figure 3: Existing *in vitro* BBB models (figure adopted from Booth et al., 2012). (a) Transwell systems which are static, vertical side-by-side diffusion systems[15]. (b) Dynamic *in vitro* (DIV) models are macro dynamic models which contains hollow fibres with micro pores that are suspended in a chamber[14]. (c) Microfluidic models are micro dynamic devices with microengineered channels that provide realistic dimensions and geometries comparable to the physiological BBB[15].

1.2 Objectives

The goal of this project is to create a device used for screening novel, GBM specific immunoPET radiotracers in their early-stage development. The device should provide a measure of how well immunoPET radiotracers cross an in vitro BBB model which can then be used to predict how well it crosses the human BBB *in vivo*. To realise this goal, the device will be comprised of (i) a microfluidic system acting as an in vitro BBB model and (ii) an integrable sensing unit.

(i) The microfluidic system aims to recapitulate healthy *in vivo* BBB permeability properties by selectively incorporating the aspects integral to establishing its permeability. Flow-induced SS, endothelial cells and the capacity for co-culture with astrocytes and pericytes will be core facets of this system. Using a healthy model ensures that immunoPET radiotracers can traverse all parts of the heterogenous BBTB. However, cells that can be perturbed to reflect the reduced paracellular barrier integrity in GBM is desirable.

(ii) The sensing unit should eliminate the necessity for additional measurement procedures, such as microscopy. The integrated sensors should provide data which can be used to estimate the amount of immunoPET radiotracer that traverses the *in vitro* BBB model. This will be done by detecting gamma photons emitted by immunoPET radiotracers or fluorescence from fluorophore conjugated immunoPET radiotracers, which makes this device unique.

Through these methods, this device aims to match the time and cost efficiency of current Transwell models whilst benefitting from the more accurate physiological representation that microfluidic models provide. **Error! Reference source not found.**

Table 1: Success criteria for each objective based on literature on current models.

RMT denotes receptor-mediate transcytosis. AMT is adsorptive-mediated transcytosis. ABC-family efflux transporters denote ATP-binding cassette family efflux transporters. EC for endothelial cells. Transepithelial electrical resistance (TEER). Fluorescein Isothiocyanate (FITC dextran). GBM denotes glioblastoma multiforme and BBB for blood-brain-barrier. PET in immunoPET stands for positron emission tomography.

Objective	Aspect	Criteria
Accurate BBB permeability function	BBB physiology	- Cells that express receptors present on human BCECs capable of RMT - Cells that permit AMT - Cells that form a confluent monolayer with tight junctions that inhibit paracellular transport across the endothelium. - Cells that express ABC-family efflux transporters
	GBM	- Include cells that can be perturbed to achieve reduced paracellular barrier integrity. - An information relay system that can detect the degree of barrier tightness.
	Microfluidic chip	- Apply shear stress ≥1dyn/cm^2 to EC cells during in chip culture - Achieve a TEER value ≥150Ωcm2 - Prevent FITC-dextran 70kDa dextran with permeability co-efficient of 10^{-5}
Integrated ImmunoPET Sensing Unit	ImmunoPET detection	- Detect 511keV gamma photons
	Information relay	- Output data that can be used to calculate immunoPET concentrations
Utility, Quality, Value adding	Additional Features	- An all-in-one product that provides additional features of: mimicking different GBM conditions and obtainment of immunoPET radiotracer permeability to the BBB.

2. Methods

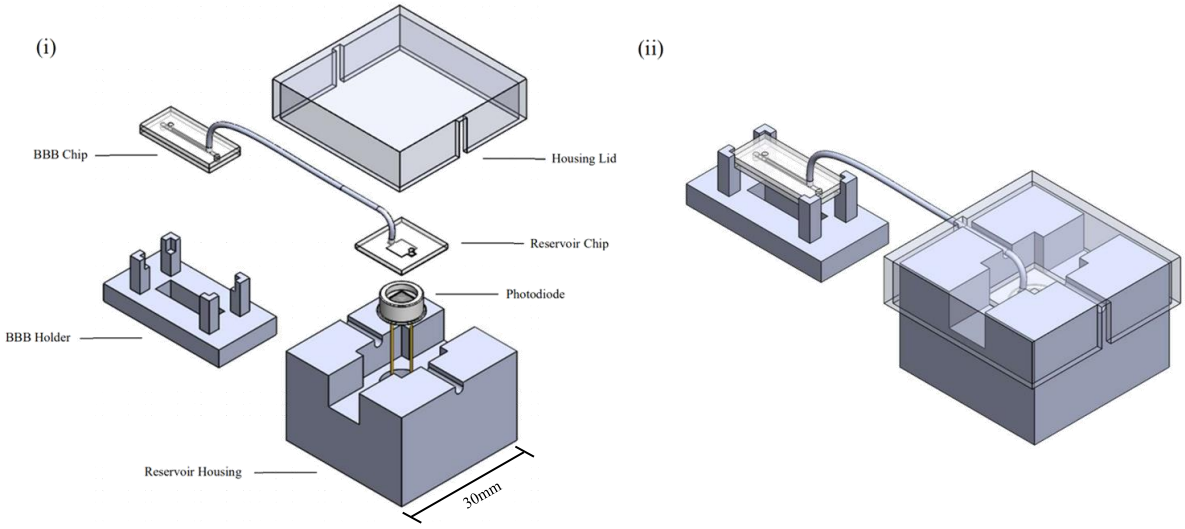

Figure 4: (i) Device design exploded view with measurement for reference, (ii) Device design assembly. Only the tube connecting the BBB chip to the reservoir is shown here but, there will be tubing in all inlets/outlets. The cap has been made translucent for viewing purposes. All design done in SolidWorks.

The device consists of: (1) BBB chip holder with BBB chip and (2) reservoir housing containing photodiode sensing system with reservoir chip (Figure 4). The BBB holder allows insertion of tubing into both sides of the chip. The BBB chip contains the model barrier, consisting of a membrane with cells cultured on it, that separates the blood and brain channels and allows the transport of molecules between the two channels. The reservoir housing aligns the reservoir of the reservoir chip directly above the photodiode at a constant distance. The lid is opaque to prevent external light from reaching the photodiode, reducing noise.

An immunoPET radiotracer is first flowed into the blood channel of the BBB chip which represents a capillary. Flow is then stopped, and immunoPET diffuses across the barrier under static conditions. After some time, the brain channel contents of the BBB chip are pumped into the reservoir, where the photodiode sensing system detects the amount of immunoPET that has crossed the barrier, allowing an estimation of immunoPET permeability coefficient in the physiological BBB.

2.1 Chip

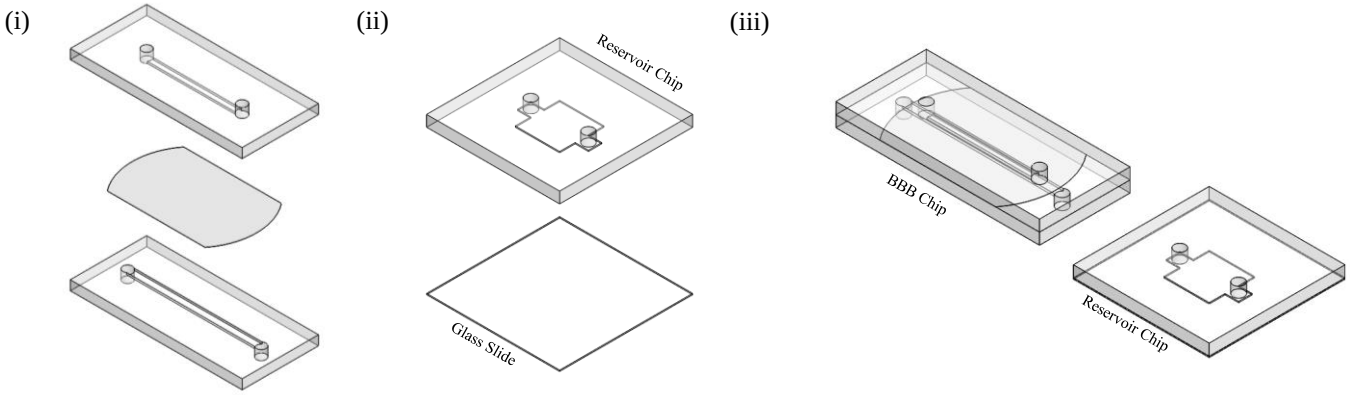

Figure 5: (i) Exploded view of the BBB chip, which shows a 0.4µm diameter polycarbonate membrane sandwiched between 2 PDMS chip layers, with one layer containing the brain channel and the other the blood channel., (ii) Exploded view of the reservoir chip containing the reservoir, made up of a PDMS chip layer covered by a glass slide, (iii) View of assembly of BBB chip and reservoir chip

Overview of Chip Design

There are two chips, the BBB chip and the reservoir chip (Figure 5). The BBB chip consists of the blood channel, brain channel and polycarbonate (PC) membrane (VWR, #516-4509). Membranes with pore size 0.4 µm provide the best barrier integrity from a range of pore sizes[19]. Both components have inlets to allow input of cells, medium and immunoPET radiotracers, and outlets for extraction of waste (blood channel) and samples for testing (brain channel). It is necessary to remove the fluid from the brain channel to detect immunoPET because any immunoPET left in the blood channel would cause interference with the photodiode sensing system. The reservoir chip stores extracted brain channel fluid for sensing.

The dimension of each feature is in Table 1. Limited by the 13mm diameter PC membrane, the length of the brain channel is 10mm. The blood channel is longer to ensure more uniform flow at the interface (intersection of blood and brain). The dimensions of the reservoir are determined by the area needed by the photodiode to detect the radiotracer.

Table 1: Channel and reservoir dimensions of the BBB chip and the reservoir chip respectively.

	Height (µm)	Width (µm)	Length (mm)
Blood Channel	200	800	14
Brain Channel	200	640	10
Reservoir	100	4000	4000

Fabrication of Chips

To make the chips, a negative mould was created. Since all features in Table 2 are in the 100µm range, the high-resolution mould weas fabricated using an SLA printer. The chip material is PDMS because PDMS is high resolution, optically transparent and biocompatible[20]. PDMS was prepared by using a 9:1 elastomer to curing agent ratio. It was then degassed and poured into sterilised moulds to set

for 3-4 hours at 70ºC on a hot plate. Once the inlets and outlets were hole-punched with a 1mm diameter biopsy punch, the PDMS was removed from the mould. To seal off the channels, the chips and cover slips were placed in a plasma cleaner for 4 minutes and then pressed together to form a tight seal.

2.2 Cells

Reagents were purchased from Sigma-Aldrich unless otherwise stated. HeLa and cell-free experiments served as the negative cellular and negative acellular control for all dextran perfusion studies and calcein-AM and F-actin staining experiments.

2.2.1 Cell Culture

Human umbilical vein endothelium cells (HUVECs) from (ATCC, CRL-1730™) were cultured using manufacturer protocol in 75cm^2 flasks (T-75s) with a complete endothelium growth medium (EGM) consisting of F-12K + 10% fetal bovine serum (FBS) + 0.1mg/mL heparin + 30µg/mL endothelial cell growth supplement (ECGS)(Fisher Scientific, United Kingdom). The cell medium was changed every 48 hours and the cells were maintained in a 37˚C incubator at 5% CO_2. Subculture of cells was taken once 80% confluency had been reached and cells were detached from the T-75 flasks using trypsin-EDTA.

HeLa cells were cultured according to manufacturer protocol in T-75s using a cell culture medium consisting of DMEM + 10% FBS.

2.2.2 Cell Seeding

Calcein staining (discussed in 2.2.5) observations were recorded at 4, 24, 48, 72 and 96 hours after seeding.

Static

PC membranes were prepared for cell seeding by coating with a diluted (10µg/mL) extra cellular matrix (ECM) of Collagen I Rat protein or human plasma fibronectin and allowing 100µL of cell medium to absorb whilst incubating at 37˚C, 5% CO_2. HUVECs were seeded onto PC membranes at 15000 cells/cm^2, HeLa at 6000 cells/cm^2 and both incubated under static conditions.

Shear

Cell seeding within the channel can be achieved by flowing ECM through the blood channel and leaving to adhere statically in the incubator for 3 hours. HUVECs are flowed through the blood channel and cultured for 1 hour under static conditions and then maintained for a further 3 hours under very low flow rate (≤0.1µL/min). The flow rate is then increased to 7µL/min for the next 92 hours.

2.2.3 Treatment cyclic AMP

The protocol outlined in section 2.2.2 is repeated with the addition of 8-(4-Chlorophenylthio)adenosine-3′,5′-cyclic monophosphate sodium salt (pCPT-cAMP) (Sigma-Aldrich, United Kingdom). pCPT-cAMP is a cell membrane permeable form of the nucleotide cyclic adenosine monophosphate (cAMP)[21].

To investigate cAMP, HUVECs are seeded into the microfluidic device and cultured in EGM until 100% confluence is achieved. HUVECs are treated with pCPT-cAMP from 4 hours after cell seeding at concentrations of 0.5, 25, 50, 200 and 250µg/mL. Permeability experiments are performed after confluence is achieved (as discussed in 2.2.4). Treatment concentrations and durations for pCPT-cAMP were informed by a previous study by Ho et al., 2017[21].

2.2.4 Functional analyses of Barrier Integrity

Dextran permeability assays

Fluorescent tracer molecules of different molecular sizes were used to assess endothelial monolayer permeability[21][22]. Permeability assays were conducted after 4 days of endothelial cell culture in the BBB chip under shear stress. Prior to permeability experiments, Fluorescein Isothiocyanate (FITC) tagged 10kDa Dextrans (Sigma-Aldrich, 51923) and Texas Red tagged 70kDa Dextrans (Invitrogen, D1864) were each reconstituted in endothelial growth medium at 500µg/mL. The dextran solution was loaded into the blood channel of the BBB chip then left for 6 hours without shear flow to allow dextran molecules to diffuse through the barrier. Samples were then collected from the brain channel. The fluorescence intensities of the original dextran solution and the sample collected from the brain channel were recorded with a multi-channel fluorescence plate reader and compared to calculate the permeability coefficient for each dextran (defined as the ratio of original dextran concentration to the collected sample dextran concentration)[18].

TEER

TEER can be rapidly measured using a voltohmeter through built-in electrodes in the brain and blood channels. Applying a DC voltage to these electrodes allows current measurement, enabling the resistance calculation using Ohm's Law (Equation 1). TEER value is then the calculated resistance multiplying by the area of the brain channel with units Ω·cm^2[23] (Equation 2).

$$R_m = \frac{V}{I} \tag{1}$$

R_m: Resistance of membrane
V : Applied voltage
I : Measured current

$$TEER = R_m \cdot A \tag{2}$$

R_m: Resistance of membrane
A: Area in which brain and blood channels overlap

2.2.5 Expression analyses

Expression analyses were conducted with calein-AM (Invitrogen, C3099), a membrane permeable stain used to evaluate cell viability and Phalloidin-iFluor 555 Reagent (Abcam, ab176756), an F-actin-binding phalloidin dye conjugate. During cell seeding experiments, calcein-AM was used as a surrogate to investigate formation prior to validation with Phalloidin-iFluor 555 Reagent F-Actin staining. When staining in the microfluidic chip, stain was flushed through the blood channel using a pipette tip.

Calcein-AM Stains

Using EGM, calcein-AM was diluted to 5µM. HUVEC and HeLa cells were then stained with 80µl/cm^2 and incubated for 60 minutes at 37^{o}C and 5% CO2. Cells were then imaged with an ECLIPSE Ti2 inverted microscope (Nikon, UK).

Immunocytochemistry

HUVEC and HeLa cells were then fixed in 3.7% formaldehyde solution in PBS for 10 minutes, followed by three washes with PBS. Cells were then permeabilised in 0.2% Triton X-100 solution for 5 minutes, followed by three washes with PBS. Cells were stained with Phalloidin-iFluor 555 Reagent. Cells were then imaged with an ECLIPSE Ti2 inverted microscope (Nikon, UK).

2.2.6 Quantification and statistical analysis of cellular monolayers

ImageJ (FIJI) will be used for quantitative analysis of junctional proteins. Fluorescence intensity will be calculated in ImageJ. Comparisons between HeLa (negative control) and HUVEC cells will be computed using unpaired Student t tests in GraphPad Prism. $P<0.05$ will be considered statistically significant. All experiments, cellular and acellular controls will be repeated twice to ensure reproducibility.

2.3 ImmunoPET Sensing

Positrons emitted from immunoPET radiotracer stored in the reservoir annihilate into 511keV gamma photons. To detect the gamma photons emitted, a photodiode will be used. To test the behaviour of the photodiode and circuitry under varying radiant flux, the circuit seen in

Error! Reference source not found. 6(i) was constructed onto a breadboard (Figure 6(ii)). The diode used was a S1223-01 Hamamatsu Full Spectrum Si photodiode and all other components were obtained from The Imperial College Advanced Hackspace. To vary the flux onto the photodiode, a blue LED emitting 450nm photons was used. The experiment was conducted in a dark room and any light emitting apparatus was turned away from the photodiode to ensure any incident light onto the photodiode was solely from the blue LED.

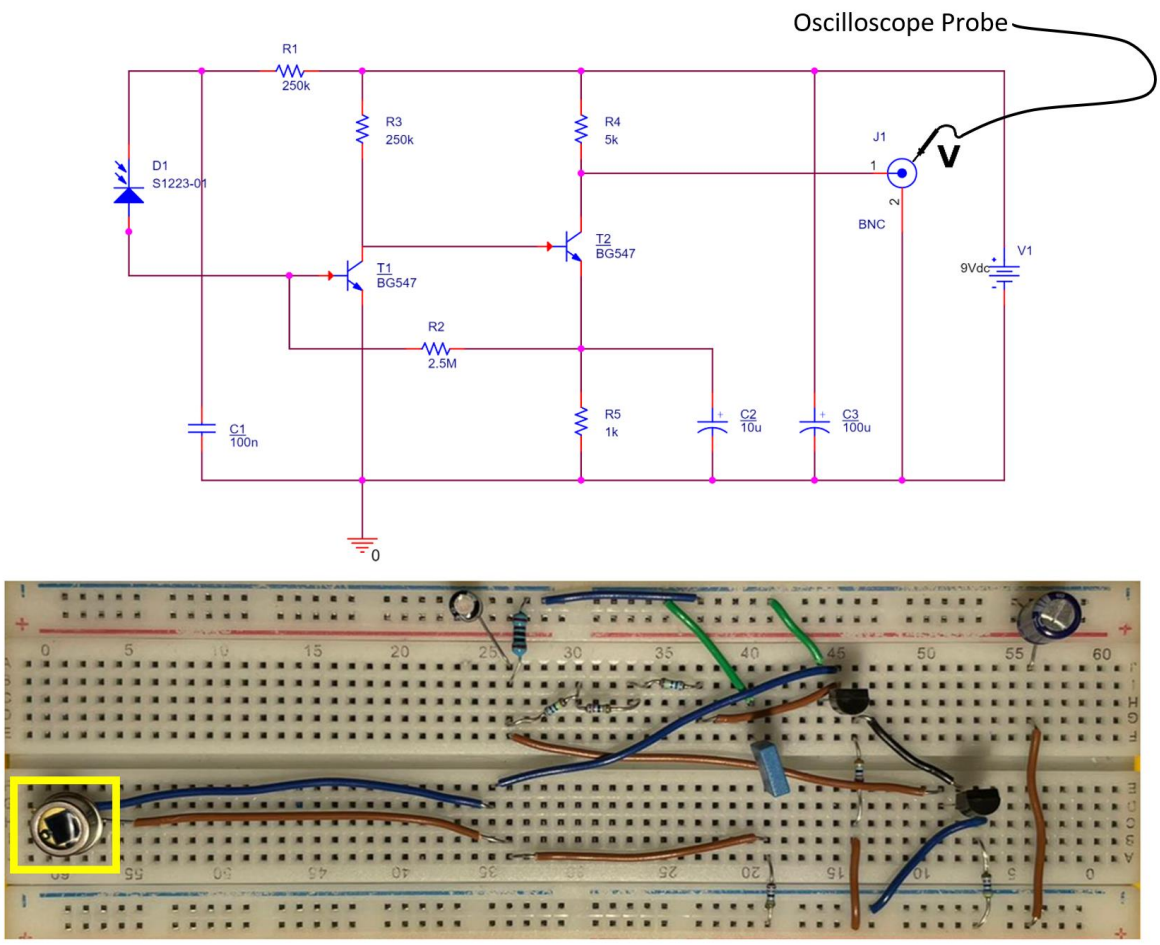

Figure 6: i) Schematic of circuit that will be used to detect 511keV gamma photons, adapted from Burkhard Kainka [24], (ii) Implementation of schematic onto a breadboard which was tested with blue LED source. Photodiode position is highlighted with a yellow box.

The LED was positioned at a fixed distance from the photodiode. They were aligned such that light strikes the photodiode surface perpendicularly (Figure 7(ii)), mimicking the reservoir being directly above the photodiode as previously shown in Figure 4. Different concentrations of immunoPET in the reservoir would result in different radiant flux incident onto the photodiode. To simulate this, the voltage across the LED was increased in 0.01V intervals using a IPS 3202 Iso-tech power supply. To observe the circuit behaviour, a T3DSO1204 digital oscilloscope was used. Its settings were adjusted for the clearest signal characterisation and the waveforms were captured using the screen capture function (Figure 7(i)). The experiment was then repeated for distances ranging from 44.28-114.22mm. Distances outside of this range would cause the LED to fail due to under or overvolting being required.

(i)

(ii)

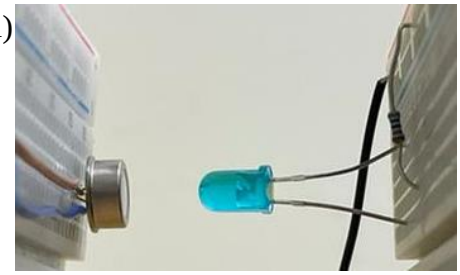

Figure 7: (i) Oscilloscope set up in DC coupling mode, rising edge triggering, vertical sensitivity of 5V per division and a time base of 1ms per division, (ii) alignment of photodiode to ensure incident light is perpendicular to photodiode surface.

The effect of reverse bias voltage across the photodiode was also tested. Under the same experimental conditions, the LED source was placed a fixed distance, 47.50mm, from the photodiode and the voltage across the photodiode was varied from 6V to 18V inclusive in 3V increments. The voltage across the LED was also varied in 0.01V increments and the observed waveforms were captured using the oscilloscope with the same settings.

3. Results

Chip

The fabricated chips are shown in Figure 8 and Figure 9. Flow tests were undertaken to test channel viability and the results is shown in Figure 10Figure . The housing pieces fabricated for the support and shielding of the two chips are shown in Figure 11.

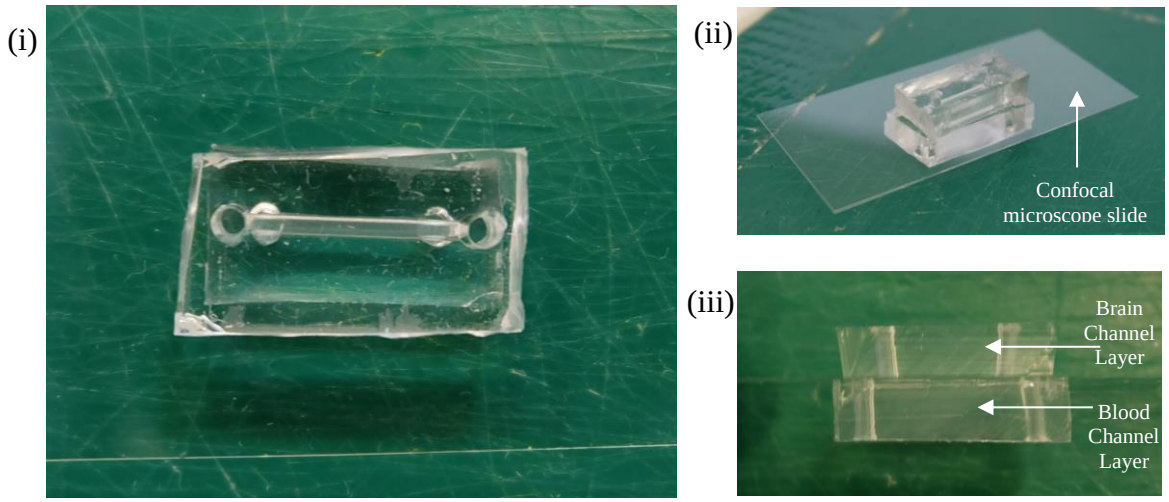

Figure 8: The fabricated BBB chip consisting of two PDMS pieces bonded onto a confocal microscope slide to demonstrate their orientation in relation to each other. (i) Bottom view. (ii) Isometric view. (iii) Front view.

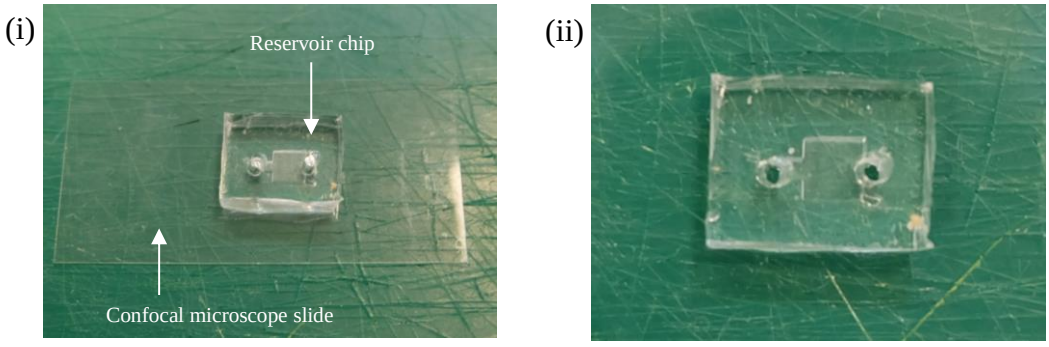

Figure 9: The Fabricated Reservoir chip consisting of a PDMS piece bonded onto a confocal microscope slide to enclose the reservoir. (i) The reservoir chip with the microscope slide attached to it. (ii) A zoomed-in image of the reservoir chip.

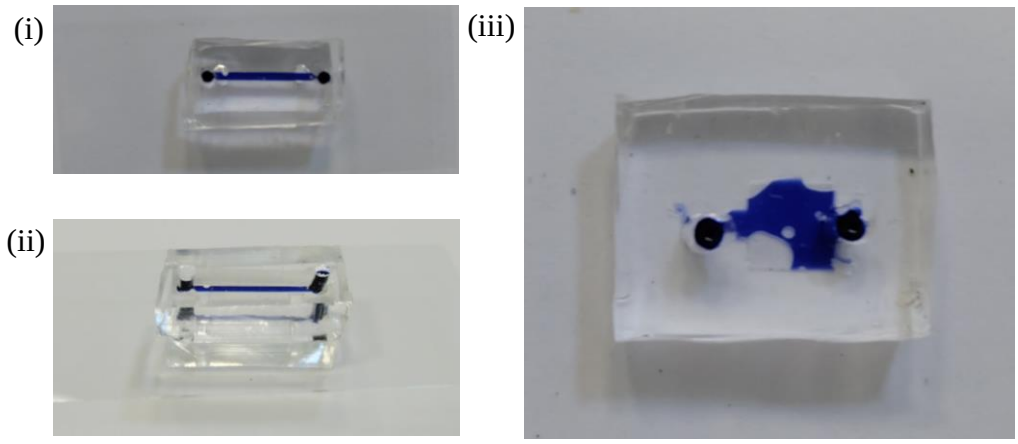

Figure 10: Results of flow test on the blood channel and reservoir using Trypan Blue solution dye with a pipette. (i) Top view of BBB chip which shows a successful flow test. (ii) Angled top view of BBB chip which shows a successful flow test. (iii) Top view of reservoir chip which shows that the reservoir chip designed need to be improved on since fluid did not cover the entire reservoir.

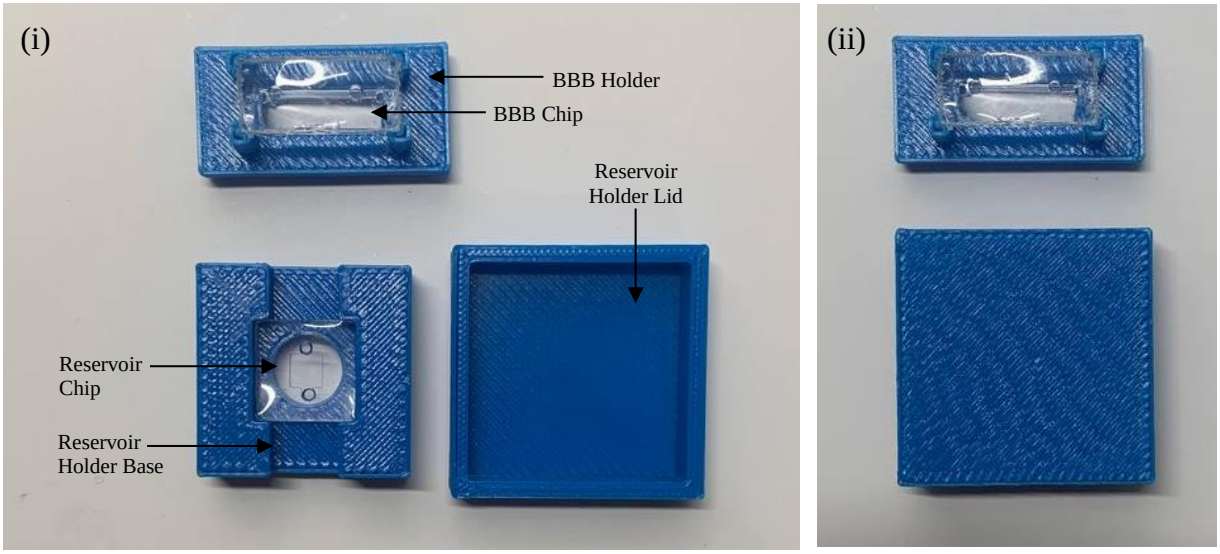

Figure 11: The housing pieces for the chips to ensure alignments and to protect the photodiode from external photon sources, with the lid off and lid on for the reservoir housing in (i) and (ii) respectively.

Cells

Expression results

Figure 12 shows the results of calcein-AM staining of negative control (HeLa) cells at 4 and 24 hours, post seeding into a T-75 under static culture conditions.

(i) 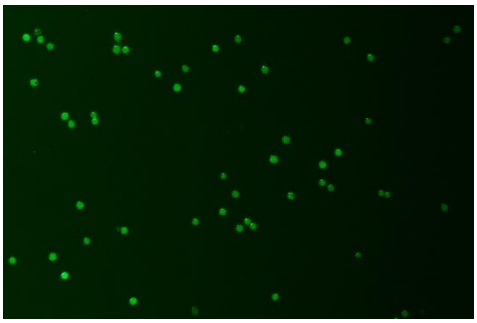 (ii) 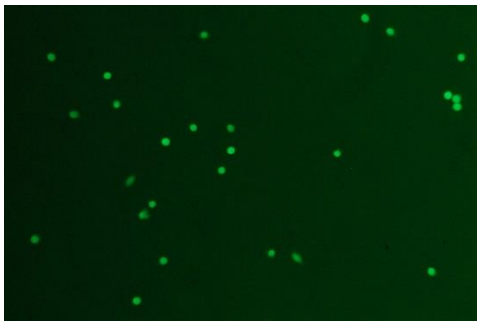

Figure 12: Fluorescent images at 10x magnification showing negative control 10x (HeLa cells) statically cultured on T75 flasks at (i) 4 hours post seeding and (ii) 24 hours post seeding

Sensing

Figure 13 shows 4 examples of waveforms captured during testing circuit and photodiode behaviour. Figures 14-16 graph the analysis performed on each waveform captured.

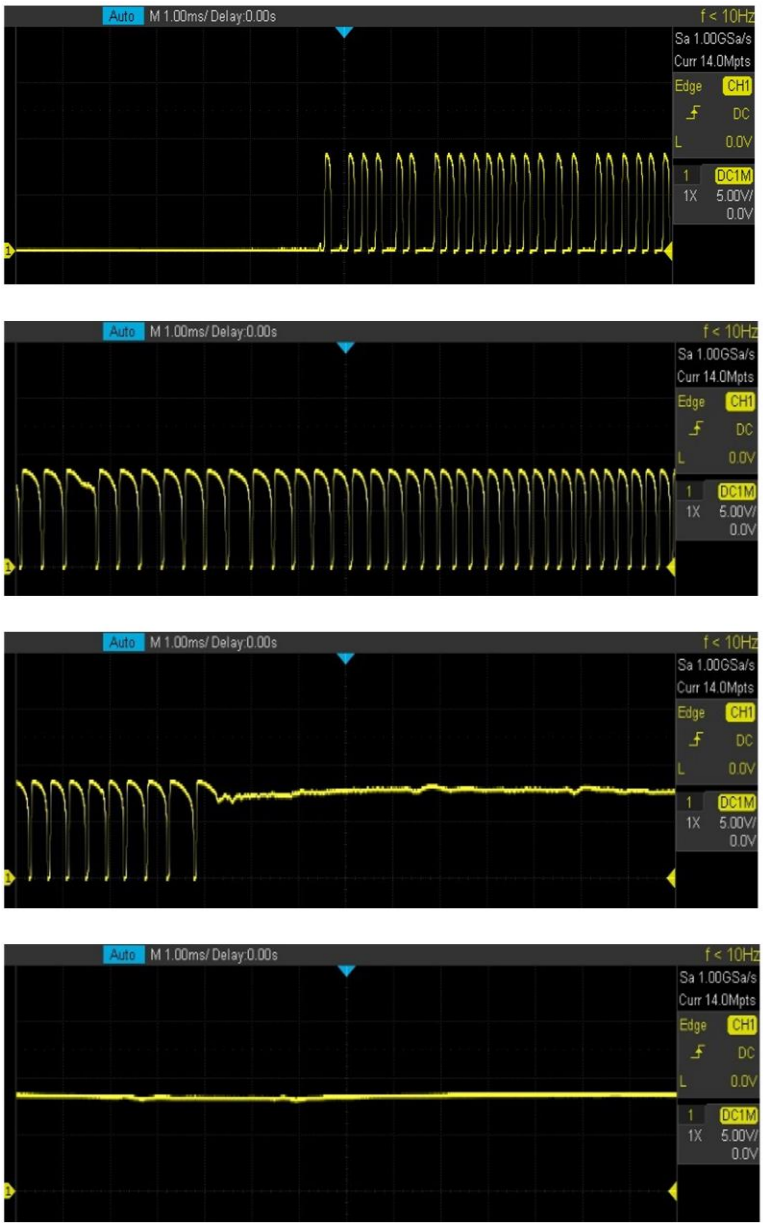

Figure 13: Four waveforms captured as radiant flux on the photodiode increases.

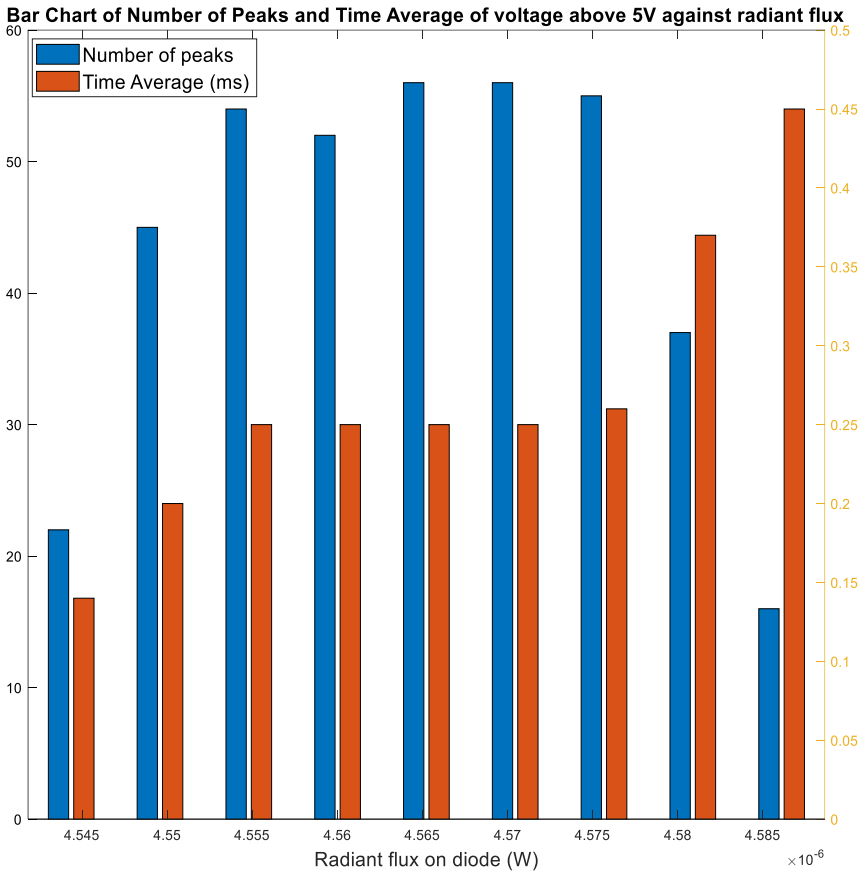

Figure 14: Bar chart indicating the number of peaks within 14ms of timeframe and time average of voltage above 5V in each peak against radiant flux on diode

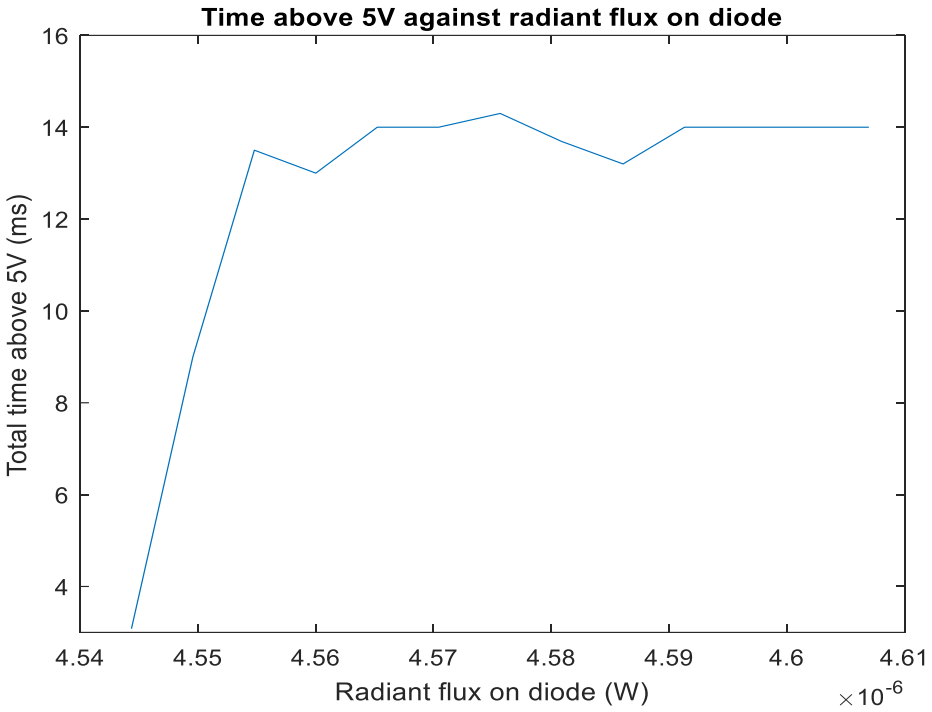

Figure 15: Total time above 5V against radiant flux at a reverse bias of 9V and a distance of 114.22mm between LED source and photodiode

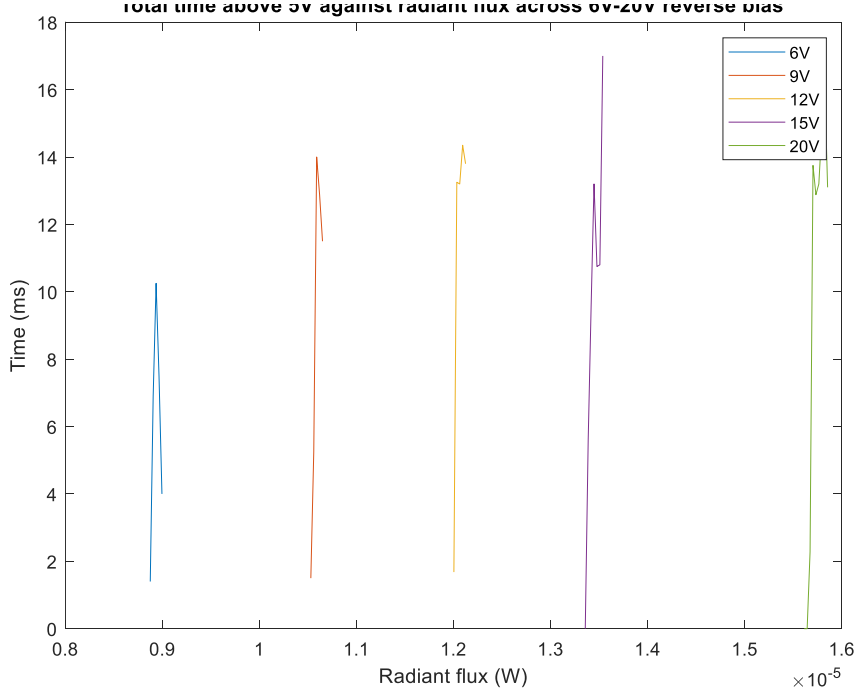

Figure 16: Total time above 5V against radiant flux across 6,9,12,15,20V reverse bias voltage across photodiode

4. Discussion

4.1 Chip

Fluid flow through the channels in the BBB chip was good whereas it could be improved for the reservoir. A reason that fluid was not able to spread over the entire reservoir could be the larger surface area and the smaller depth as compared to the channels, so surface tension is a lot higher. To overcome this issue, the reservoir can either be made deeper or designed as a continuous 'square zig-zag' channel (Figure 17).

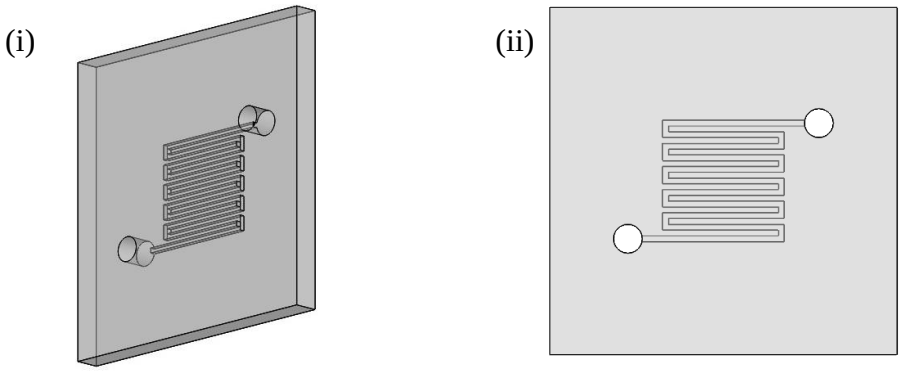

Figure 17: The reservoir chip with the 'square zig-zag' channel which maintains a general square shape with a greater depth for less surface tension and ease of punching holes. The corners at each bend can be rounded but it is not crucial because the purpose of the reservoir is solely to analyse the contents in the sample and is not affected by shear stress and hence flow. (i) An angled view of the chip. (ii) The top view of the chip.

SLA printing has provided an accurate mould because PDMS replicas took on the shape of the moulds well. If smaller channels are needed for higher shear stress to increase cell growth, photolithography could be used to improve the accuracy of small features.

The current mould has the three features (blood channel, brain channel and reservoir) combined and each chip is cut out after moulding (Figure 18(i)). The lack of markings resulted in the uneven chip sizes, which is not ideal. For the BBB chip, it makes it difficult to align the blood and brain channels. For the reservoir chip, size of the chip and position of the reservoir is crucial since the reservoir needs to fit nicely above the photodiode. Moreover, the shallow reservoir made punching of the inlets difficult because it was hard to see. To improve the moulds, 3 separate moulds can be made for each layer. This was the first design but was changed as the depth and volume was too small, making handling difficult (Figure 18(ii)). For the new moulds, they will be made deeper and bigger.

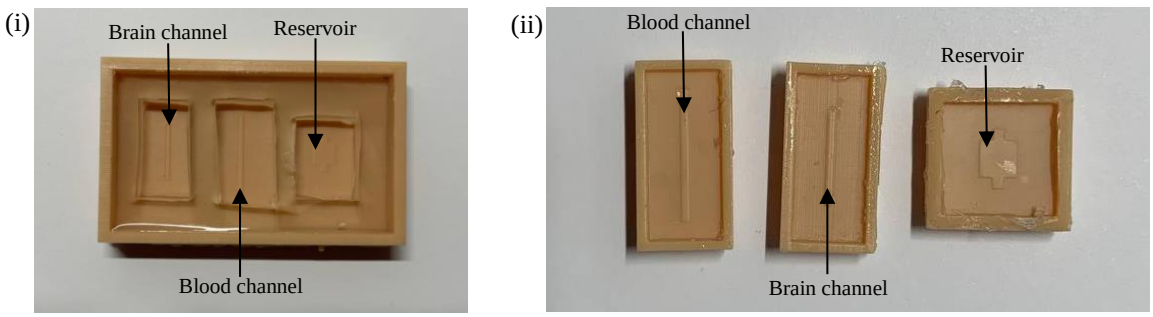

Figure 18: (i) The current mould in which the shape of each layer cut out is uneven. (ii) The original moulds which were too thin but gave the correct layer dimensions. The next mould will be fabricated in a similar manner with an increased depth and volume for the ease of handling and preparation of PDMS mixture.

4.1.1 Shear Stress

Shear stress (SS) is described by Equation (3). Two main factors affect SS: channel geometry and flow rate. With respect to the channel walls, geometry affects SS profile and flow rate affects SS value. With cylindrical channels, they better mimic the shape of capillaries, but manufacturing is difficult[25]. Rectangular channels have been reported to exhibit high barrier tightness with a TEER values as high as 2000Ω·cm^2[17]. Hence, the channels were manufactured to be rectangular.

$$\tau = \frac{6Q\eta}{h^2 w} \tag{3}$$

τ: Shear stress
Q: Flow rate
η: Dynamic viscosity
h: Channel height
w: Channel width

Channel Geometry

ECs are cultured on one longitudinal plane of the rectangular blood channel (hereinafter referred to as cultured plane). The uniformity of SS experienced at the cultured plane is affected by the aspect ratio w/h of the channel because SS varies along the width of the cross-section of the channel (Equation (4)). It is ideal for the cultured plane to have uniform SS across its width such that all ECs experience the optimal SS.

$$\tau_w(y) = \frac{4h}{\pi^2}\frac{\Delta P}{L}\sum_{n,odd}^{\infty}\frac{1}{n^2}\left[1 - \frac{\cosh\left(\frac{n\pi y}{h}\right)}{\cosh\left(\frac{n\pi w}{2h}\right)}\right] \tag{4}$$

Fluid dynamic simulations within the channel were performed using COMSOL Multiphysics®. Results show that as w/h increases, SS becomes more uniform across the width (Figure 19(i)). Hence, w/h of 4:1 is selected for the blood channel, with simulations showing that at least 77% of the channel width has $\tau \geq 80\%$ of τ_{max} (Figure 19(ii)).

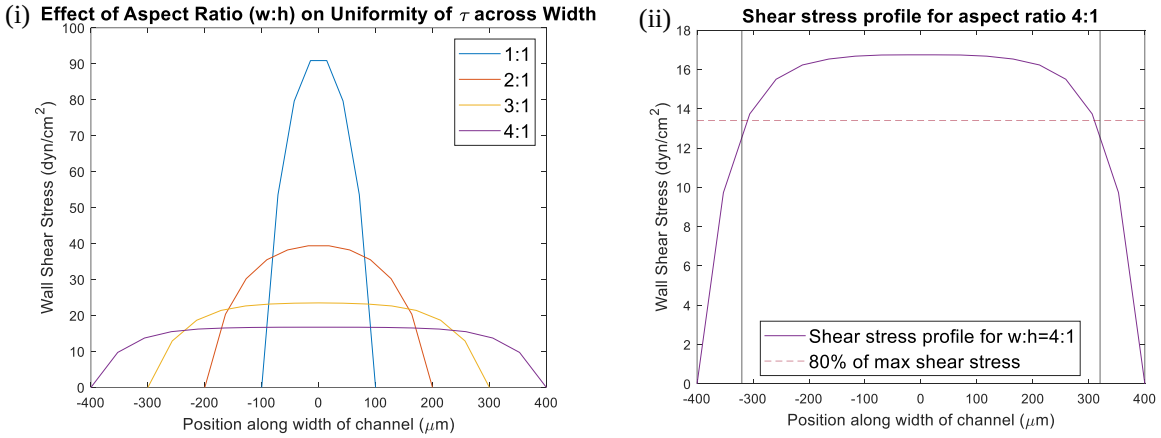

Figure 19: One-dimensional shear stress (SS) profiles across channel width, with data points obtained from COMSOL simulations and plotted with Matlab. Note that flow parameters used (such as flow rate and viscosity) does not affect the results. (i) SS profile for different aspect ratios. (ii) SS profile for an aspect ratio of 4:1. The horizontal line represents 80% of the maximum SS value. The vertical line represents the width of the brain channel and hence the interface between the blood and brain channel. It is expected that maximum cell growth will happen between the 2 vertical lines for the blood channel.

To determine the channel dimensions, existing models were referred to (Table 2) and the limits of fabrication techniques were considered. The height was thus decided to be 200 µm. Correspondingly, the width is 800µm for w/h of 4:1. To maximise the area of the blood channel that experiences at least 13.4dyn/cm^2, which is 80% of SS_{max} = 16.7 dyn/cm^2, the brain channel was made 20% narrower than the blood channel.

Table 2: Dimensions of cross-sectional area of existing models.

Width (µm)	Height (µm)	Aspect ratio	Ref.
300	160	1.875	[51]
500	100	5	[52]
1000	300	3.333	[18]
200	100	2	[53]

Flow rate

The dynamic viscosity of the fluid was assumed to be that of water of 0.69mPa·s at 37°C.The flow rate Q was calculated to be 69µL/min[1] in order to achieve a physiological shear stress level 15dyn/cm^2. SS varies proportionally with viscosity and flow rate, so a higher SS can be obtained during experiments by changing flow rate or viscosity. COMSOL simulations showed a uniform flow along the width of the channel with Q=696 µL/min, with the cross-section shown in Figure 20(i). Most of the cultured plane experienced a uniform SS of at least 14dyn/cm^2 (Figure 20 (ii)).

[1] Refer to Appendix A1 for calculations.

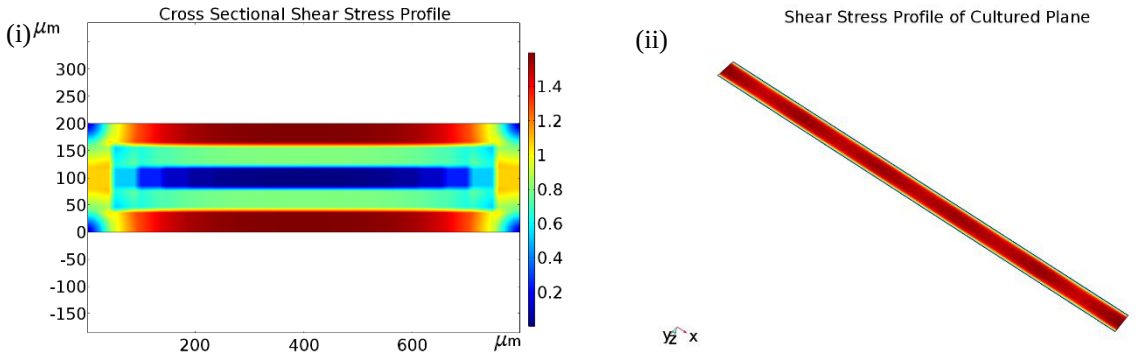

Figure 20: Shear stress profile in 2D and 3D obtained from COMSOL simulations. Note that the units for shear stress in the figures is in Pa, not dyn/cm^2. (i) Cross-sectional τ profile. (ii) τ profile across cultured plane

However, a Q value of 696µL/min is significantly higher than literature values of 0.01-120µL/min[16]. Moreover, this requires excessive cell culture medium. However, since SS minimally needs to be 1dyn/cm^2, reducing the flow rate 10 times to 7µL/min should results in SS being 1.5dyn/cm^2 because SS is directly proportional to Q. This will have to be verified through permeability studies using dextrans and TEER measurements that has yet to be performed due to time constraints.

4.1.2 Laminar Flow

It is valid to assume laminar fluid flow in the channels. With the small length scale in microfluidics, viscous forces dominate inertial forces. According to Equation (5), this means Reynold's number Re is small. Re was calculated to be 14.7 for the blood channel, hence laminar flow can be safely assumed since flows are turbulent if Re>2000.

$$Re = \frac{inertial\ forces}{viscous\ forces} = \frac{\rho v L}{\mu} \quad (5)$$

ρ: Fluid density
v: Fluid Velocity
L: Channel length
µ: Dynamic viscosity

4.1.5 Further improvements

Membrane Type

An artificial membrane, like the PC membrane used in this model, is much thicker than the physiological membrane resulting in in less cell-to-cell interaction. A 'membraneless' BBB chip can be created by culturing astrocytes and endothelial cells onto a hydrogel. However, such designs greatly increase the complexity of the chip and with time constraints, an artificial membrane was used. Studies have shown that 'membraneless' designs improve barrier integrity with higher TEER values (Table 3). A planned future improvement is to create a 'membraneless' design and compare the barrier integrity with the current chip.

Table 3: TEER comparison for different membrane types. It is clear that 'membraneless' designs have higher TEER values and hence better barrier integrity, with the first 2 designs providing a direct comparison since the cell culture used is the same.

Cell Culture	Design Type	TEER Value	Ref.
Primary rat BMECs and Astrocytes	Membraneless	1298 $\Omega \cdot cm^2$	[26]
Primary rat BMECs and Astrocytes	PET Membrane	114.2 $\Omega \cdot cm^2$	[27]
HCMEC/D3 cell line and p5-p7 human astrocytes	Membraneless	1000 $\Omega \cdot cm^2$	[28]
bEnd.3 cell line and C6 Astrocyte cell line	Polycarbonate Membrane	223-280 $\Omega \cdot cm^2$	[29]

Implementation of Electrodes

Since barrier tightness will be varied to mimic different GBM conditions, electrodes provide a fast way to evaluate barrier tightness and hence the environment different studies require through TEER measurement. Examples of built-in electrodes is in Figure 21(i). Due to time constraints; the electrodes have not been built but a prospective design is shown in Figure 21 (ii).

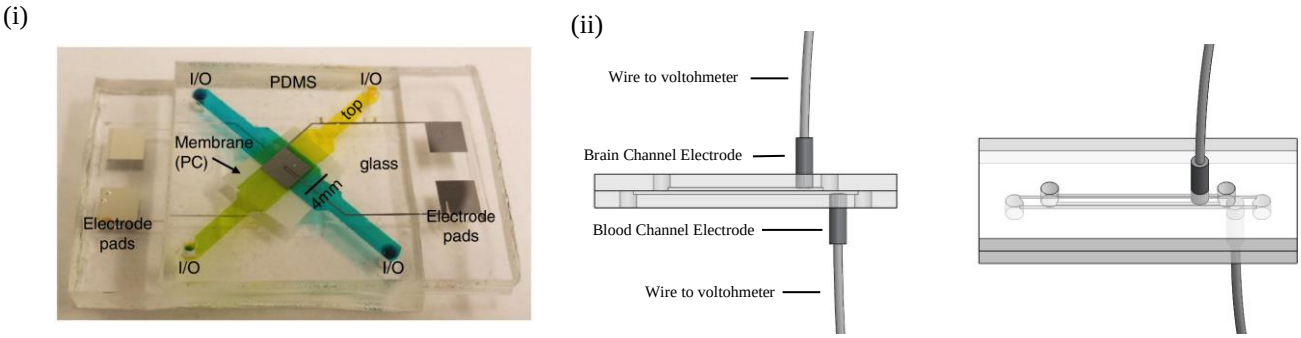

Figure 21: (i) Example of microfluidic chip with electrodes built into the upper and lower channel allowing for a direct TEER measurement taken from Booth et al.[29], (ii) Prospective design for the implementation of electrodes into our current chip design

4.2 Cells

4.2.1 Endothelial Cell Selection

Incorporation of mammalian endothelial cells into the in vitro BBB microfluidic chip confers characteristics of the BBB observed in vivo, generating a physiologically representative model [10]. There are various sources of endothelial cells each with distinct properties[10][30-33]. Among these, the human BCEC cell line hCMEC/d3 is widely used to model the human BBB in vitro due to its thorough characterisation, accurate physiological representation of primary human BCECs and negation of the laborious requirements of primary cell extraction[10][34].

As hCMEC/d3 and other human BCEC cell lines were unavailable, alternative cell lines were evaluated against the project objectives. HUVECs were decided upon as the preferable cell line. The HUVEC cell line is derived from the umbilical vein vascular endothelium of a health female[42] and retains several of the advantages of human BCEC cell lines over alternative sources (i.e., primary and non-human BCECs). HUVEC is well-characterised cell line[30-33] avoiding the source-specific heterogeneity associated with primary cells[34]. In addition, HUVECs more accurately model the physiology of the human BCECs than non-human cell lines[34] and share several characteristics of primary human BCECs. A comparison between HUVECs and primary human BCECs for properties pertinent to BBB permeability screening studies is summarised in Table 5.

Table 5. The properties of cells pertinent to BBB permeability screening studies are compared in human umbilical vein endothelial cells (HUVECs)) [(ATCC® CRL-1730™)] and primary human brain capillary endothelial cells (BCECs). *Contact inhibition strongly inhibits cell proliferation restricting growth density to a single confluent monolayer, which accurate recapitulates the one cell thick BBB endothelia in vivo[9][33]. **Tight junction complexity and continuity depends on experimental conditions and can be augmented by treatment with pharmacological agents, shear stress and co-culture[21][41]. † derived from 70kDa fluorescence dextran perfusion studies measured in engineered microfluidic vasculature[30].
Pe denotes permeability coefficient. ABC-family efflux transporters denote ATP-binding cassette family efflux transporters. MDR1 denotes multidrug resistance protein 1. BCRP denotes breast cancer resistance protein. MRP denotes multidrug resistance protein. MDR1, BCRP, MRP1, MRP3, MRP4 and MRP5 are ABC-family efflux transporters[10].
RMT denotes receptor-mediate transcytosis. TfR is the transferrin receptor. IR is the insulin receptor. IGF receptor is the insulin-like growth factor receptor. LEPR is the leptin receptor[13]. TfR, IR, IGF receptor, LEPR and scavenger receptors are the receptors present in the human BBB in vivo capable of RMT[13].

Property	Primary human BCEC	HUVEC	Ref.
Contact inhibition	Exhibit contact inhibition*	Exhibit contact inhibition*	[9, 33]
Tight junctions	Present**	Present**	[22]
ABC-family efflux transporters	Express MDR1, BCRP, MRP1, MRP3, MRP4 and MRP5	Express BCRP, MRP1, MRP4 and MRP5	[32]
Monolayer barrier integrity	$Pe = 0.910 \pm 0.405 \times 10^{-7}$ cm/s †	$Pe = 2.743 \pm 0.550 \times 10^{-7}$ cm/s †	[30]
RMT transporters	Express TfR, IR, IGF receptor, LEPR, scavenger receptors	Express TfR, IR, IGF receptor, LEPR, scavenger receptors	[36-40]

4.2.2 HUVEC as a Model of the Brain Microvasculature

Endothelial cells such as HUVECs that share functional characteristics of the BBB may be useful surrogates to investigate BBB permeability[40], especially where human BCEC cell lines are unavailable. As noted in Table 5, HUVECs exhibit certain phenotypic differences to primary human BCECs[10][33][35], notably a reduced monolayer barrier integrity. However, there are experimental perturbations that can ameliorate the barrier functionality of HUVEC endothelia to better recapitulate that of the human BBB in vivo[21]. These are summarised in Table 6. The authors' upcoming experiments will evaluate how well HUVECs can approximate the functionality of the native BBB when cultured under shear stress, cAMP treatment or both. While could not be acquired, pericyte-HUVEC co-culture represents a potential future improvement to our device.

Table 6. Experimental conditions that can improve the barrier integrity of human umbilical vein endothelial cell (HUVEC) monolayers. Pe denotes permeability coefficient. LY denotes Lucifer Yellow. TJ denotes tight junction. cAMP denotes cyclic adenosine monophosphate.

Experimental condition	Effect on HUVECs	Ref.
Microfluidic-simulated shear stress	Pe = 3.50×10^{-5} cm/s (10kDa dextrans) Pe = 2.47 × 10−5 cm/s (70kDa dextrans)	[21]
Treatment with cAMP	Concentration dependent decreases in 10kDa and 70kDa dextran permeability coefficients*	[21]
	Stimulated tight and adherens junction expression	[21]
HUVEC-pericyte co-culture	Reduction in LY Pe from 2.35 ± 0.54 x 10^{-3}cm/min in monoculture to 0.96 ± 0.12 x 10^{-3} cm/min in coculture	[41]
	Improved continuity of ZO-1 and Claudin-5 in TJ protein immunostaining at cell-cell junctions.	[41]

4.2.3 Cellular Experiments

At the time of writing, HUVECs had not achieved sufficient confluence to undergo splitting and seeding into either static or dynamic culture condition experiments. The negative control (HeLa) cells had achieved sufficient confluence and have been seeded for static culture condition experiments. Upcoming experiments will first validate that HUVECs form confluent monolayers in static culture conditions. Culture in T75 flasks will be compared to culture on the collagen-treated PC membrane to ensure that confluent monolayers can form on the PC membrane. Once validated, cells will be cultured in dynamic conditions in the microfluidic device as described in section 2.2.2.

4.3 Sensing

4.3.1 Sensitivity

Sensitivity is a measure of the smallest detectable signal by a system. The sensitivity of the circuit to gamma photons could not be tested directly in initial experiments. Thus, testing methods revolved around varying radiant flux onto the photodiode using a blue LED, which also provides an indication of sensitivity[43]. There are large dissimilarities in the behaviour of photodiodes, regarding energy transduction, between visible and gamma photons. The greatest disparity is in quantum efficiency, defined as the percentage probability that an incident photon will generate a detectable electron in a detector[44]. Additionally, the photodiodes spectral response is undefined for wavelengths less than 300nm (Figure 22) whilst the detection target has a wavelength of 2.4pm. Therefore, predicting realistic circuit behaviour without using a gamma photon source is not possible. However, our results did show that measurements obtained from this circuit can be used to determine immunoPET radiotracer concentrations in the reservoir chip.

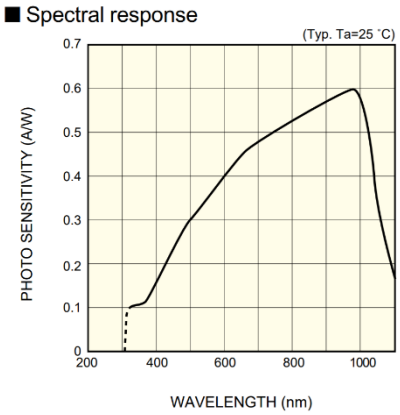

Figure 22: A graph to show how the photosensitivity of the photodiode varies across different wavelengths. As seen, the curve is not defined below 300nm wavelengths. Ref [45]

4.3.2 Determining ImmunoPET concentrations

Figure 15 shows that beyond a radiant flux of 4.57μW, the voltage remained above 5V for at least 93% of the 14ms timeframe of each signal. This indicates that immunoPET concentrations that result in radiant fluxes higher than 4.57μW will not be distinguishable. Extrapolating from the linear region of Figure 15 at lower fluxes, the lower concentration limit can also be calculated. Calculations performed on these results (Appendix B2) show that the concentration range of the current circuit is $6.98 \times 10^{-2} - 7.02 \times 10^{-2} \rho mol/mm^3$. The physical interpretation of this data does not relate to scenarios likely to occur in the system, based on concentrations observed in literature[46]. In future testing, using a gamma source and performing the same calculations, a meaningful concentration range could be determined.

4.3.3 Adjusting Sensitivity

If, after obtaining the detectable concentration range using a gamma source, the minimum detectable concentration is too high, there are two changes that can be easily implemented to increase the sensitivity of the circuit. Firstly, multiple photodiodes can be connected in parallel as this would generate larger currents as long as the increased diode area resulted in larger total fluxes[47]. Secondly, the photodiode used could be replaced for one that has a scintillator. A scintillator luminesces when excited by ionising radiation and through this process, increases the quantum efficiency of photodiodes up to 14-fold (Figure 23). If the maximum distinguishable concentration is too low, the current amplification of the circuit could be reduced by using NPN transistors with smaller transfer ratios and altering resistor values.

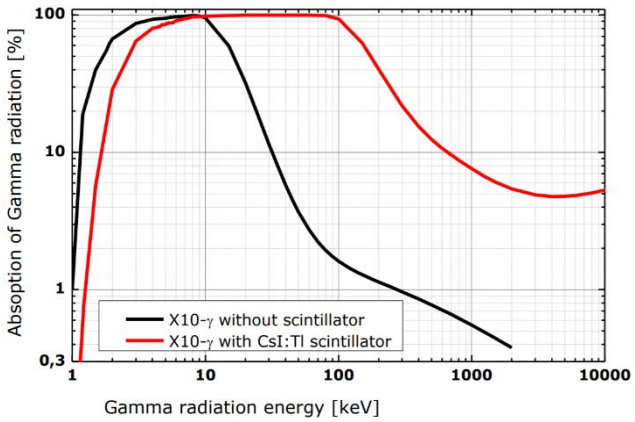

Figure 23: A logarithmic graph comparing the quantum efficiency of a photodiode with and without a scintillator across varying photon energies. The energy relevant to the success of the integrated sensing unit is 511keV[48].

4.3.4 Effect of reverse bias on sensitivity and noise

Figure 16 shows that as the reverse bias across the photodiode increases, the radiant flux required to maintain the voltage above 5V for over 10s increases. This suggests that increasing the reverse bias decreases the sensitivity, contrary to what was found in literature[49,50]. This could be explained by the increased leakage currents opposing the photocurrent as reverse bias rises[47]. The results therefore favour a lower reverse bias, but the decreased capacitance of the photodiode leads to an increase in noise[47]. An optimal reverse bias must balance sensitivity to small signals whilst limiting noise, in order to discern between gamma photons and noise.

4.3.5 Calibration Curve

To quickly relate the output signal of the sensing circuit to immunoPET concentrations in the reservoir, a calibration curve can be created as described in Appendix B3.

4.4 Blood Brain Tumour Barrier

The ability of immunoPET agents to traverse the BBTB may differ from that across the physiological BBB due to the reduced integrity of the BBTB[8]. Therefore, the ability to create a BBB microfluidic device in which the permeability is tuneable to either physiological BBB or pathophysiological BBTB conditions would be beneficial to immunoPET permeability screening studies.

There are three methods to reduce barrier integrity which will be investigated in this order: (1) simply reducing fluid flow rate and hence shear stress[17], (2) introducing cAMP[21] and (3) introducing the proinflammatory factor thrombin[30]. By varying the amount of either of the 3 methods used, the TEER value and tracer flux permeability coefficient at each amount can be measured and a calibration

curve can be plotted. The user can thus refer to this curve to obtain the desired barrier tightness needed for BBTB analysis.

4. Conclusion

The successful fabrication of the chips and promising advancements in our cell work indicates that we will be able to achieve a number of the success criteria, such as attaining the shear stress goal and identifying cells that feature several of the transcellular and paracellular transport systems relevant to BBB permeability present in vivo. Upcoming experiments will measure addition parameters such as TEER and tracer molecule permeability coefficients to further evaluate the remaining success criteria.

We demonstrated that the output of the photodiode sensing system can provide data which can be used to back-calculate immunoPET concentrations. Further testing with gamma photons will give an even more realistic view of how this sensing circuit will perform within the context of the whole device.

Once individual testing has been completed, we hope to fully integrate the different aspects of our design and test the capabilities of the device as a whole.

5. References

[1] Kumar P, Clark M. *Kumar and Clark's Clinical Medicine*. 9th ed. The Netherlands: Elsevier; 2016.

[2] Hanif F, Muzaffar K, Perveen K, Malhi SM, Simjee SU. Glioblastoma Multiforme: A Review of its Epidemiology and Pathogenesis through Clinical Presentation and Treatment. *Asian Pacific Journal of Cancer Prevention*. 2017;18(1): 3-9. Available from: doi: 10.22034/APJCP.2017.18.1.3.

[3] Tamimi AF, Juweid M. Epidemiology and Outcome of Glioblastoma. In: De Vleeschouwer S, editor. Glioblastoma [Internet]. Brisbane (AU): Codon Publications; 2017 Sep 27. Chapter 8, doi: 10.15586/codon.glioblastoma.2017.ch8

[4] Wolff A, Antfolk M, Brodin B, Tenje M. In Vitro Blood–Brain Barrier Models—An Overview of Established Models and New Microfluidic Approaches. *Journal of Pharmaceutical Sciences*. 2015;104(9): 2727-2746. Available from: doi: 10.1002/jps.24329

[5] Ene CI, Holland EC. Personalized medicine for gliomas. *Surg Neurol Int*. 2015;6(Suppl 1): S89-95. Available from: doi:10.4103/2152-7806.151351.

[6] Hernandez R, Sun H, England CG, Valdovinos HF, Barnhart TE, Yang Y, Cai W. ImmunoPET Imaging of CD146 Expression in Malignant Brain Tumors. *Mol Pharm*. 2016;13(7):2563-70. Available from: doi: 10.1021/acs.molpharmaceut.6b00372

[7] Fu R, Carroll L, Yahioglu G, Aboagye EO, Miller PW. Antibody Fragment and Affibody ImmunoPET Imaging Agents: Radiolabelling Strategies and Applications. *ChemMedChem*. 2018;13(23): 2466. Available from: doi: 10.1002/cmdc.201800624.

[8] Arvanitis CD, Ferraro GB, Jain RK. The blood–brain barrier and blood–tumour barrier in brain tumours and metastases. *Nature Reviews Cancer*. 2020; 20: 26-41. Available from: doi: 10.1038/s41568-019-0205-x

[9] Sweeney MD, Zhao Z, Montagne A, Nelson AR, Zlokovic BV. Blood-Brain Barrier: From Physiology to Disease and Back. *Physiological Reviews*. 2019;99(1): 21-78. Available from: doi: 10.1152/physrev.00050.2017

[10] Helms HC, Abbott NJ, Burek M, Cecchelli R, Couraud PO, Deli MA, et al. In vitro models of the blood-brain barrier: An overview of commonly used brain endothelial cell culture models and guidelines for their use. *Journal of Cerebral Blood Flow and Metabolism*. 2016;36(5): 862-90. Available from: doi: 10.1177/0271678X16630991.

[11] Luissint AC, Artus C, Glacial F, Ganeshamoorthy K, Couraud PO. Tight junctions at the blood brain barrier: physiological architecture and disease-associated dysregulation. *Fluids Barriers CNS*. 2012;9(1):23. Available from: doi: 10.1186/2045-8118-9-23.

[12] Löscher W, Potschka H. Blood-brain barrier active efflux transporters: ATP-binding cassette gene family. Available from: *NeuroRx.* 2005;2(1):86-98. Available from: doi: 10.1602/neurorx.2.1.86.

[13] Chacko AM, Li C, Pryma DA, Brem S, Coukos G, Muzykantov VR. Targeted delivery of antibody-based therapeutic and imaging agents to CNS tumors: Crossing the blood-brain-barrier divide. Expert Opinion Drug Delivery. 2013;10(7): 907-926. Available from: doi:10.1517/17425247.2013.808184

[14] Booth R, Kim H. Characterization of a microfluidic in vitro model of the blood-brain barrier (μBBB). Lab on a Chip. 2012;12(10): 1784-1792. Available from: 10.1039/c2lc40094d

[15] Sivandzade F, Cucullo L. In-vitro blood–brain barrier modeling: A review of modern and fast-advancing technologies. Journal of Cerebral Blood Flow & Metabolism. 2018;38(10): 1667-1681. Available from: doi: 10.1177/0271678X18788769

[16] Jiang L, Li S, Zheng J, Li Y, Huang H. Recent Progress in Microfluidic Models of the Blood-Brain Barrier. Micromachines (Basel). 2019;10(6): 375. Available from: doi: 10.3390/mi10060375

[17] Wong A, Ye M, Levy A, Rothstein J, Bergles D, Searson P. The blood-brain barrier: an engineering perspective. Frontiers in Neuroengineering. 2013;6(7). Available from: doi: 10.3389/fneng.2013.00007

[18] Jeong S, Kim S, Buonocore J, Park J, Welsh C, Li J et al. A Three-Dimensional Arrayed Microfluidic Blood–Brain Barrier Model With Integrated Electrical Sensor Array. *IEEE Transactions on Biomedical Engineering*. 2018;65(2):431-439. Available from: doi: 10.1109/TBME.2017.2773463

[19] Wuest D, Wing A, Lee K. Membrane configuration optimization for a murine in vitro blood–brain barrier model. *Journal of Neuroscience Methods*. 2013;212(2): 211-221. Available from: doi: 10.1016/j.jneumeth.2012.10.016

[20] Gale, B.K.; Jafek, A.R.; Lambert, C.J.; Goenner, B.L.; Moghimifam, H.; Nze, U.C.; Kamarapu, S.K. A Review of Current Methods in Microfluidic Device Fabrication and Future Commercialization Prospects. *Inventions.* 2018;3(60). Available from: doi: 10.3390/inventions3030060

[21] Ho YT, Adriani G, Beyer S, Nhan PT, Kamm RD, Kah JCY. A Facile Method to Probe the Vascular Permeability of Nanoparticles in Nanomedicine Applications. *Sci Rep*. 2017;7(1):707. Available from: doi: 10.1038/s41598-017-00750-3.

[22] Jeong S, Kim S, Buonocore J, Park J, Welsh CJ, Li J, et al. A Three-Dimensional Arrayed Microfluidic Blood-Brain Barrier Model With Integrated Electrical Sensor Array. *IEEE Trans Biomed Eng*. 2018;65(2): 431-439. Available from: doi: 10.1109/TBME.2017.2773463.

[23] Srinivasan B, Kolli AR, Esch MB, Abaci HE, Shuler ML, Hickman JJ. TEER measurement techniques for in vitro barrier model systems. *J Lab Autom.* 2015;20(2):107-126. Available from: doi: 10.1177/2211068214561025

[24] Burkhard Kainka. Measure gamma rays with a photodiode: Radiation detector using a BPW34. Available from: http://atom.univ.kiev.ua/2016/prof/yerm/prog_logic/presentations/khodnevych.pdf [Accessed 16th March 2021]

[25] Oddo A, Peng B, Tong Z, Wei Y, Tong W, Thissen H et al. Advances in Microfluidic Blood–Brain Barrier (BBB) Models. *Trends in Biotechnology*. 2019;37(12):1295-1314. Available from: doi: 10.1016/j.tibtech.2019.04.006

[26] Xu H, Li Z, Yu Y, Sizdahkhani S, Ho WS, Yin F, Wang L, Zhu G, Zhang M, Jiang L, Zhuang Z, Qin J. A dynamic in vivo-like organotypic blood-brain barrier model to probe metastatic brain tumors. *Sci Rep*. 2016;6:36670. Available from: doi: 10.1038/srep36670

[27] Fruzsina R. Walter, Sándor Valkai, András Kincses, András Petneházi, Tamás Czeller, Szilvia Veszelka, Pál Ormos, Mária A. Deli, András Dér. A versatile lab-on-a-chip tool for modeling biological barriers. *Sensors and Actuators B: Chemical.* 2016;222:1209-19. Available from: doi: 10.1016/j.snb.2015.07.110

[28] Paul P. Partyka, George A. Godsey, John R. Galie, Mary C. Kosciuk, Nimish K. Acharya, Robert G. Nagele, Peter A. Galie. Mechanical stress regulates transport in a compliant 3D model of the blood-brain barrier. *Biomaterials.* 2017;115:30-39. Available from: doi: 10.1016/j.biomaterials.2016.11.012

[29] Booth, R., Kim, H. Permeability Analysis of Neuroactive Drugs Through a Dynamic Microfluidic *In Vitro* Blood–Brain Barrier Model. *Ann Biomed Eng. 2014;*42: 2379–91. Available from doi: 10.1007/s10439-014-1086-5

[30] Uwamori H, Ono Y, Yamashita T, Arai K, Sudo R. Comparison of organ-specific endothelial cells in terms of microvascular formation and endothelial barrier functions. *Microvasc Res*. 2019;122: 60-70. Available from: doi: 10.1016/j.mvr.2018.11.007.

[31] Drolez A, Vandenhaute E, Julien S, Gosselet F, Burchell J, Cecchelli R, et al. Selection of a Relevant In Vitro Blood-Brain Barrier Model to Investigate Pro-Metastatic Features of Human Breast Cancer Cell Lines. *PLoS One*. 2016;11(3):e0151155. Available from: doi: 10.1371/journal.pone.0151155.

[32] Dauchy S, Miller F, Couraud PO, Weaver RJ, Weksler B, Romero IA, et al. Expression and transcriptional regulation of ABC transporters and cytochromes P450 in hCMEC/D3 human cerebral microvascular endothelial cells. *Biochem Pharmacol*. 2009;77(5):897-909. Available from: doi: 10.1016/j.bcp.2008.11.001.

[33] Medina-Leyte DJ, Dominguez-Perez M, Mercado I, Villarreal-Molina MT, Jacobo-Albavera L. Use of Human Umbilical Vein Endothelial Cells (HUVEC) as a Model to Study Cardiovascular Disease: A Review. *Appl. Sci*. 2020;*10*(3): 938. Available from: https://doi.org/10.3390/app10030938

[34] Poller B, Gutmann H, Krähenbühl S, Weksler B, Romero I, Couraud PO, et al. The human brain endothelial cell line hCMEC/D3 as a human blood-brain barrier model for drug transport studies. *J Neurochem*. 2008;107(5):1358-68. Available from: doi: 10.1111/j.1471-4159.2008.05730.x.

[35] Ito S, Oishi M, Ogata S, Uemura T, Couraud PO, Masuda T, et al. Identification of Cell-Surface Proteins Endocytosed by Human Brain Microvascular Endothelial Cells In Vitro. *Pharmaceutics*. 2020;12(6):579. Available from: doi: 10.3390/pharmaceutics12060579.

[36] Bakhashab S, Lary S, Ahmed F, Schulten H, Bashir A, Ahmed F et al. Reference Genes for Expression Studies in Hypoxia and Hyperglycemia Models in Human Umbilical Vein Endothelial Cells. *G3: Genes, Genomes, Genetics*. 2014;4(11):2159-65. Available from: doi: 10.1534/g3.114.013102

[37] Nigris V, Pujadas G, Sala L, Testa R, Genovese S, Ceriello A. Short-term high glucose exposure impairs insulin signaling in endothelial cells. *Cardiovascular Diabetology*. 2015;14(114). Available from: doi:10.1186/s12933-015-0278-0

[38] Bid H, Zhan J, Phelps D, Kurmasheva R, Houghton P. Potent inhibition of angiogenesis by the IGF-1 receptor-targeting antibody SCH717454 is reversed by IGF-2. *Mol Cancer Ther*. 2012;11(3): 649-59. Available from: 10.1158/1535-7163.MCT-11-0575

[39] Arlier S. Endothelial cell leptin receptors, leptin and interleukin-8 in the pathogenesis of preeclampsia: An in-vitro study. *Turk J Obstet Gynecol*. 2017;14(4):220-227. Available from: doi: 10.4274/tjod.78545

[40] Adachi H, Tsujimoto M. Characterization of the Human Gene Encoding the Scavenger Receptor Expressed by Endothelial Cell and Its Regulation by a Novel Transcription Factor, Endothelial Zinc Finger Protein-2*. *Journal of Biological Chemistry*. 2002;227(27):24014-21. Available from: doi: 10.1074/jbc.M201854200

[41] Man S, Ubogu E, Williams K, Tucky B, Callahan M, Ransohoff R. Human Brain Microvascular Endothelial Cells and Umbilical Vein Endothelial Cells Differentially Facilitate Leukocyte Recruitment and Utilize Chemokines for T Cell Migration. *Clin Dev Immunol*. 2008;384982. Available from: doi: 10.1155/2008/384982

[42] ATCC. *HUV-EC-C [HUVEC] (ATCC® CRL-1730™)*. [Internet] Available from: https://www.lgcstandards-atcc.org/products/all/CRL-1730.aspx?geo_country=gb#generalinformation

[43] Wei-Chih Wang. Department of Power Mechanical Engineering, National Tsing Hua University, Lecture: Optical Detectors, slide 3. Available from: https://depts.washington.edu/mictech/optics/me557/detector.pdf

[44] Shim, Jong-In & Shin, Dong-Soo. Measuring the internal quantum efficiency of light-emitting diodes: Towards accurate and reliable room-temperature characterization. *Nanophotonics*. 2018;t(10),1601-15. Available from: doi: 10.1515/nanoph-2018-0094

[45] Si PIN photodiode, S1223 series datasheet. Available from: https://docs.rs-online.com/ec2b/0900766b80d838f0.pdf

[46] Reddy S, Robinson MK. Immuno-positron emission tomography in cancer models. *Semin Nucl Med*. 2010;40(3):182-189. Available from: doi: 10.1053/j.semnuclmed.2009.12.004

[47] Build and Test of A Gamma Radiation Detector by Juan Rodríguez, B.S.E.E A Thesis In Electrical Engineering. Available from: https://ttu-ir.tdl.org/bitstream/handle/2346/58537/RODRIGUEZ-THESIS-2014.pdf

[48] Silicon Photodiodes For Gamma Ray Detection, Dr. Marc Oliver Schillgalies, Spet,13,2011, available from: https://www.first-sensor.com/cms/upload/datasheets/gamma-ray-detection.pdf

[49] Photodiode Characteristics and Applications , Optoelectronics , available from: http://www.osioptoelectronics.com/application-notes/an-photodiode-parameters-characteristics.pdf

[50] Photodiode Basics, Wavelength Electronics, available from: https://www.teamwavelength.com/photodiode-basics/#:~:text=When%20reverse%20biased%2C%20current%20will,the%20maximum%20amount%20of%20photons

[51] Wang Y, Abaci H, Shuler M. Microfluidic blood-brain barrier model provides in vivo-like barrier properties for drug permeability screening. *Biotechnology and Bioengineering*. 2016;114(1):184-194. Available from: doi: 10.1002/bit.26045

[52] Griep L, Wolbers F, de Wagenaar B, ter Braak P, Weksler B, Romero I et al. BBB ON CHIP: microfluidic platform to mechanically and biochemically modulate blood-brain barrier function. *Biomedical Microdevices*. 2012;15(1):145-150. Available from: doi: 10.1007/s10544-012-9699-7

[53] Deosarkar S, Prabhakarpandian B, Wang B, Sheffield J, Krynska B, Kiani M. A Novel Dynamic Neonatal Blood-Brain Barrier on a Chip. *PLOS ONE*. 2015;10(11):e0142725. Available from: doi: 10.1371/journal.pone.0142725

Appendix A – Microfluidic Calculations

A1 Flow Rate Calculations

The flow rate Q to use for the blood channel can be determined from the equation for shear stress τ. The shear stress for the optimal growth of endothelial cells is $\tau = 15\ \text{dyn/cm}^2 = 1.5\ \text{Pa}$.

$$\tau = \frac{6Q\mu}{h^2 w}$$

τ: Shear stress
Q: Flow rate
μ: Dynamic viscosity
h: Channel height
w: Channel width

At 37°C, water has the following property: [2]

$$\mu = 0.69\ \text{mPa} \cdot \text{s}$$

The dimensions of the cross-section of the blood channel are 0.2×0.8 mm (h × w).

Hence, Q can be calculated:

$$Q = \frac{\tau h^2 w}{6\mu} \Longrightarrow Q = 11.594\ \text{mm}^3/\text{s} = 695\ \text{mm}^3/\text{min}$$

A2 Reynold's Number and Entrance Length Calculations

Reynold's Number

Reynold's number can be calculated with the following equation:

$$Re = \frac{\rho v L}{\mu}$$

ρ: Fluid density
v: Fluid Velocity
L: Channel length
μ: Dynamic viscosity

At 37°C, water has the following properties:[2]

$$\rho = 0.9933\ \text{g/cm}^3 = 993.3\ \text{kg/m}^3$$
$$\mu = 0.69\ \text{mPa} \cdot \text{s} = 0.69 \times 10^{-3}\ \text{kg/(ms)}$$

The dimensions of the blood channel are $0.2 \times 0.8 \times 14$ mm (H × W × L).

v can be determined from flow rate Q and cross-sectional area A of the channel.

$$v = \frac{Q}{A} = \frac{Q}{H \cdot W}$$

[2] Anton Paar. *Viscosity of Water*. Available from: https://wiki.anton-paar.com/en/water/

Since $Q = 7\ \mu\text{L/min} = 7\ \text{mm}^3/\text{min}$,

$$v = 43.75\ \text{mm/min} = 0.729\ \text{mm/s}.$$

This results in $Re = 14.69$. This means that the flow is laminar in the blood channel.

Entrance Length

With this Re, the entrance length L_e can be calculated with the following equation.

$$L_e = 0.05 \cdot Re \cdot D_H$$

where D_H (hydraulic diameter) is given by:

$$D_H = \frac{2wh}{w + h}$$

This results in $L_e = 0.235\ \text{mm}$ in the blood channel.

Appendix B – ImmunoPET Photodiode Sensing System

B1 Total time spent above 5V calculations

The total time that the voltage measured above 5V was calculated by measuring the time above 5V for 5 peaks in each timeframe, calculating an average time, then multiplying it by the number of peaks in the given time frame.

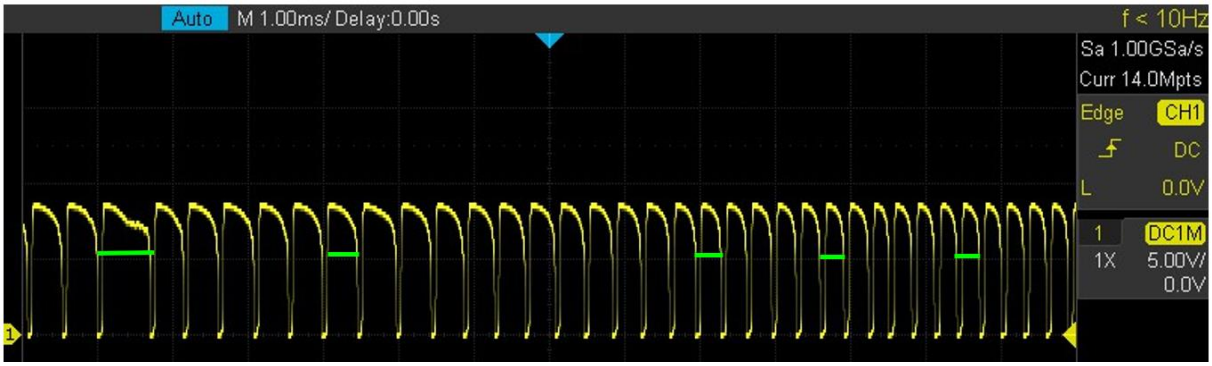

Using the above waveform as an example:
The 5 green lines highlight the peaks measured. The sum of the time across the 5 peaks is 1.7ms. The average is therefore 0.34ms. The number of peaks in this timeframe is 36. Therefore multiplying 36 by 0.34ms gives a total time above 5V of 12.24ms.

For regions where the voltage remains above 5V and no clear peaks are seen, the time of the extended region and the aforementioned method are used.

For example a waveform that looks like:

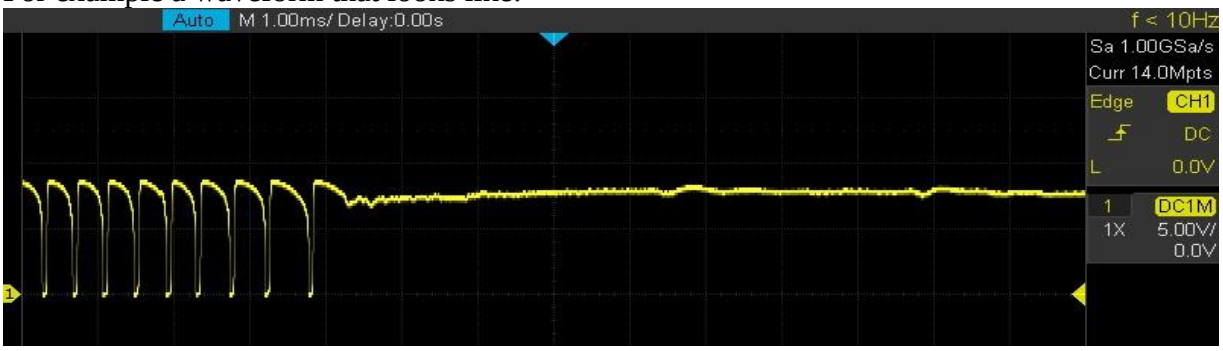

This method is better than counting the number of peaks as the number of peaks decreases as the time spent at the saturation voltage increases. Also calculating the time spent at just the saturation voltage (9V) is unviable as some peaks are at 9V only for an instant.

B2 ImmunoPET concentration calculations

The forward voltage of the LED is 3.3V

$$Current = \frac{V_{in} - V_{LED}}{500} = \frac{V_{in} - 3.3}{500}$$

$$Power = I \cdot V = \frac{V_{in} - 3.3}{500} \cdot 3.3 = \text{W}$$

By assuming a 90% power efficiency of LED, 511 keV is equivalent to 8.176×10^6 Ws

$$Radiant\ flux/Luminous\ flux = \frac{W}{r^2}$$

$$\frac{4.57\mu W}{8.176 \times 10^{-14}} = 55.8 \times 10^6 \text{ gamma photons}$$

Calculation between radiant flux on photodiode and concentration of immunoPET

For 4.57μW

$$\frac{4.57\mu W}{8.176 \times 10^{-14}} = 55.8 \times 10^6 \text{ gamma photons}$$

By assuming a photosensitivity of 0.01

$$\frac{55.8 \times 10^6}{0.01} = 5.58 \times 10^9$$

Assuming negligence of distance from source to photodiode:

$$\frac{x}{4\pi(2.5 \times 10^{-3})^2} \cdot (3.6 \times 10^{-3})^2 = 5.58 \times 10^9$$

$$x = 3.38 \times 10^{10} gamma\ photons\ from\ source$$

Assuming unidirectional emission, such that only one gamma photon will be picked up in each annihilation

$$\frac{y}{2} = 3.38 \times 10^{10}$$

$$y = 6.76 \times 10^{10} immunoPET\ molecules$$

By dividing the molecules of PET with Avogadro's number

$$\frac{6.76 \times 10^{10}}{6.02 \times 10^{23}} = 1.12 \times 10^{-13} mol$$

The volume of the reservoir is 1.6mm^3, the concentration can be calculated as follows:

$$y = \frac{1.12 \times 10^{-13} mol}{1.6 mm^3}$$

$$y = 7.02 \times 10^{-2} \rho mol/mm^3$$

For 4.54μW

$$\frac{4.54 \times 10^{-6}}{8.176 \times 10^{-14}} = 5.55 \times 10^7 gamma\ photons$$

Assuming a photosensitivity of 0.01A/W

$$\frac{5.55 \times 10^7}{0.01} = 5.55 \times 10^9 gamma\ photons$$

Let x be the number of gamma photons from source, multiplied by the size of the photodiode

$$\frac{x}{4\pi(2.5 \times 10^{-3})^2} \cdot (3.6 \times 10^{-3})^2 = 5.55 \times 10^9$$

$$x = 3.36 \times 10^{10}$$

Assuming unidirectional emission, let y be the number of molecules of immunoPET

$$\frac{y}{2} = 3.36 \times 10^{10}$$

$$y = 6.72 \times 10^{10} molecules\ of\ PET$$

By dividing the molecules of PET with Avogadro's number

$$\frac{6.72 \times 10^{10}}{6.02 \times 10^{23}} = 1.11 \times 10^{-13} mol$$

The volume of the reservoir is 1.6mm^3, the concentration can be calculated as follows:

$$y = \frac{1.11 \times 10^{-13} mol}{1.6 mm^3}$$

$$y = 6.98 \times 10^{-2} \rho mol/mm^3$$

B3 calibration curve

To create a calibration curve, known concentrations of immunoPET should be put into the reservoir. The integrated sensing system should be used to capture waveforms at each concentration. Each waveform should then be analysed to find the total time spent above 5V using the method described in Appendix B1. A plot of the time spent above 5V against the immunoPET concentration can then be produced with a appropriate line of best fit. The calibration curve should then be referred to when analysing the waveform of practical experiments to find unknown concentrations.